REPUBLIC OF TURKEY
ADANA ALPARSLAN TÜRKEŞ SCIENCE AND TECHNOLOGY UNIVERSITY

INSTITUTE OF GRADUATE STUDIES
DEPARTMENT OF ELECTRICAL ELECTRONICS ENGINEERING

DETECTION OF MCF-7 BREAST CANCER CELLS AND MONITORING OF AREA, RADIUS, AND PERIMETER DEVELOPMENTS OF THEM IN DIFFERENT DAYS

CİHAT EDİZ AKBABA
MASTER OF SCIENCE

REPUBLIC OF TURKEY

ADANA 2021

ADANA ALPARSLAN TÜRKEŞ SCIENCE AND TECHNOLOGY UNIVERSITY

INSTITUTE OF GRADUATE STUDIES
DEPARTMENT OF ELECTRICAL ELECTRONICS ENGINEERING

DETECTION OF MCF-7 BREAST CANCER CELLS AND MONITORING OF AREA, RADIUS, AND PERIMETER DEVELOPMENTS OF THEM IN DIFFERENT DAYS

CİHAT EDİZ AKBABA
MASTER OF SCIENCE

SUPERVISOR
Asst. Prof. Dr. ADEM POLAT

ADANA 2021

I hereby declare that all information in this thesis has been obtained and presented in accordance with academic rules and ethical conduct. I also declare that, as required by these rules and conduct, I have fully cited and referenced all information that is not original to this work.

Cihat Ediz AKBABA

ABSTRACT

DETECTION OF MCF-7 BREAST CANCER CELLS AND MONITORING OF AREA, RADIUS, AND PERIMETER DEVELOPMENTS OF THEM IN DIFFERENT DAYS

Cihat Ediz AKBABA

Department of Electrical Electronics Engineering

Supervisor: Asst. Prof. Dr. Adem POLAT

January 2021, 53 pages

Breast cancer is the most common cancer among women. In the world, these cells need to be analyzed well in order to develop effective treatment methods against cancer cells. In this study, image processing techniques were applied to breast cancer cells called MCF-7 cultured in the Lab-on-a-chip environment, and their development on 3 different days was examined. 3dimensional images of breast cancer cells within spheroid used in the study were obtained with an optical-based imaging tool called mini-Opto tomography platform. Images containing threedimensional spheroid structures were separated into two-dimensional layers with the ImageJ program before processing, and the images belonging to these layers were subjected to three main processes. In the first step, the pre-processing was performed on the images and with this operation, the disorders in the images were eliminated with the help of various filters and the images were adapted to the segmentation step. The main purpose of the segmentation step is to separate the main tumor masses in the spheroid structure from the image background. For this, the main tumor masses was brought to the fore by applying the thresholding, various morphological, and contour operations. The next step after the segmentation step is the “feature extraction” step that numerical data were obtained from some geometric properties of main tumor masses such as area, perimeter, and radius. As a result of the main operations applied to the images, the boundaries of the main tumor masses were drawn automatically and successful results were obtained compared to the manual drawings. When analyzed the volumetric development of 3-dimensional cancerous structures for three different days, the main tumor mass has grown approximately 121.72 percent from the second day to the fourth day and approximately 85.80 percent from the fourth day to the sixth day. These growth rates indicate that the main tumor masses used in the study tend to grow continuously. The data obtained from the MCF-7 breast cancer cells used in the study are very important for the volumetric development of cancer cells and for the classification processes that will be used in determining the type of cancer in the following stages. In the thesis study, using Python programming language and open source OpenCV library, early detection of cancer cells and a good analysis of their properties are very important in terms of providing clear and detailed information to experts. This information provided to the experts is vital in increasing the success of the treatment with early diagnosis, avoiding unnecessary biopsies, and reducing the time that the specialists interpret cancerous images.

Keywords: breast cancer detection, biomedical image processing, medical image segmentation, breast cancer, computer-aided image analysis.

ÖZET

MCF-7 MEME KANSERİ HÜCRELERİNİN TESPİTİ VE FARKLI GÜNLERDE ALAN, YARIÇAP VE ÇEVRE GELİŞİMLERİNİN İZLENMESİ

Cihat Ediz AKBABA
Elektrik Elektronik Mühendisliği Anabilim Dalı
Danışman: Dr. Öğr. Üyesi Adem POLAT
Ocak 2021, 53 sayfa

Meme kanseri, kadınlarda görülen kanser türleri arasında en yaygın olanıdır. Dünyada, kanserli hücrelere karşı etkili tedavi yöntemlerinin geliştirilmesi için, bu hücrelerin iyi bir şekilde analiz edilmesi gerekmektedir. Yapılan çalışmada, lab-on-a-chip ortamında kültürlenen MCF-7 adı verilen meme kanseri hücreleri üzerinde görüntü işleme teknikleri uygulanarak bu hücrelerin 3 farklı gündeki gelişimleri incelenmiştir. Çalışmada kullanılan spheroiddeki meme kanseri hücrelerinin üç boyutlu görüntüleri mini-Opto tomografi platformu adı verilen optik tabanlı bir görüntüleme cihazıyla elde edilmiştir. Üç boyutlu spheroid yapılarını içeren görüntüler işlenmeden önce ImageJ programı ile iki boyutlu katmanlara ayrılmıştır ve katmanlı görüntüler üç ana işleme tabi tutulmuştur. İlk olarak görüntüler üzerinde ön işleme adımı gerçekleştirilmiştir. Bu işlemle görüntü içerisindeki bozukluklar çeşitli filtreler yardımıyla giderilmiştir ve görüntüler segmentasyon adımına uygun hale getirilmiştir. Segmentasyon adımında ana amaç spheroid yapısı içerisindeki ana tümör kitlelerini görüntü arka planından ayırmaktır. Bunun için eşikleme işlemi, çeşitli morfolojik işlemler ve contour işlemleri uygulanarak ana tümör kitleleri ön plana çıkarılmıştır. Segmentasyondan sonraki adım ise ana tümör kitlelerinin alan, çevre ve yarıçap gibi bazı geometrik özelliklerinden sayısal verilerin elde edildiği "özellik çıkarma" adımıdır. Görüntüler üzerinde uygulanan ana işlemler sonucunda ana tümör kitlelerinin konturları otomatik olarak çizdirilmiştir ve manuel yapılan çizimlerle karşılaştırıldığında başarılı sonuçlar elde edilmiştir. Üç farklı gün için 3 boyutlu

kanserli yapıların hacimsel gelişimleri incelendiğinde ana tümör kitlesi ikinci günden dördüncü güne kadar yaklaşık olarak yüzde 121.72 ve dördüncü günden altıncı güne yaklaşık yüzde 85.80 lik bir büyüme göstermiştir. Bu durum ana tümör kitlesinin sürekli bir şekilde büyüme eğiliminde olduğunu göstermektedir. Çalışmada kullanılan MCF-7 meme kanseri hücrelerinden elde edilen veriler kanser hücrelerinin hacimsel gelişimleri ve ilerleyen aşamalarda kanser türünü belirlemede kullanılacak olan sınıflandırma işlemleri için oldukça önemlidir. Yapılan tez çalışmasında görüntüler üzerinde Python programlama dili ve açık kaynak kodlu OpenCV ortamı kullanılarak kanser hücrelerinin erken tespiti ve özelliklerinin iyi bir şekilde analiz edilmesiyle uzmanlara net ve detaylı bilgiler sunmak oldukça önemlidir. Uzmanlara sunulan bu bilgiler erken teşhisle tedavinin başarısını arttırmada, gereksiz biyopsilerden kaçınmada ve uzmanların kanserli görüntüleri yorumlama süresini azaltmada hayati öneme sahiptir.

Anahtar Kelimeler: meme kanseri tespiti, biyomedikal görüntü işleme, medikal görüntü segmentasyonu, meme kanseri, bilgisayar destekli görüntü analizi.

To my family.

ACKNOWLEDGEMENTS

I would like to express my deepest gratitude to my supervisor Asst. Prof. Dr. Adem POLAT for his devoted guidance, suggestions and support. He always encouraged me and gave me the opportunity for valuable academic experiences.

I am deeply grateful to all the jury members for agreeing to read my thesis and to participate in the defense of this thesis.

Finally, I would like to thank my family for their endless support and love. I will be forever grateful to them.

TABLE OF CONTENTS

TABLE OF CONTENTS xii
LIST OF FIGURES xiii
LIST OF TABLES xvi
1. INTRODUCTION 1
1.1. Breast Cancer 2
1.2. Breast Cancer Imaging Methods 3
1.2.1. Mammography 3
1.2.2. Digital Breast Tomosynthesis 3
1.2.3. Ultrasound 4
1.2.4. Magnetic Resonance Imaging 4
1.3. Scope of The Thesis 5
1.3.1. Computer-Aided Image Processing Systems 6
1.3.2. Mini Opto Tomograpy Platform 6
1.3.3. Algebric Reconstruction Technique 7
1.3.4. MCF-7 Cells 8
1.3.5. Light Microscopy 8
2. LITERATURE REVIEW 10
3. MATERIALS AND METHODS 13
3.1. Image Acqusition 15
3.2. Preprocessing 16
3.2.1. RGB to GRAY Transformation 17
3.2.2. Image Filtering 19
3.2.2.1. Mean Filter 20
3.2.2.2. Median Filter 21
3.2.2.3. Bilateral Filter 23
3.2.2.4. Gaussian Filter 24
3.3. Segmentation 27
3.3.1. Thresholding Process 28
3.3.2. Morphological Operations 32

3.3.2.1. Dilation 32
3.3.2.2. Erosion 33
3.3.2.3. Opening and Closing 33
3.3.3. Contour Tracking 35
3.3.4. Edge Detection 37
3.4. Feature Extraction 38
3.4.1. Contour Area Calculation 38
3.4.2. Contour Length Calculation 39
3.4.3. Diameter Drawing 39
4. RESULTS AND DISCUSSIONS 40
4.1. Area Measurements 41
4.2. Perimeter Measurements 43
4.3. Radius Measurements 45
5. CONCLUSIONS 47
6. RECOMMENDATIONS 48
REFERENCES 49
CURRICULUM VITAE 53

LIST OF FIGURES

Figure 1.1. The estimated cancer types and mortality rates by gender in United States, in 2019. 1
Figure 1.2. The death rates due to breast cancer in women between the ages of 40-84 in the USA from 1969 to 2019 (Hendrick et al., 2019). 2
Figure 1.3. General structure of digital breast tomosynthesis (Schulze-Hagen, Eshghi, Müller, & Müller-Leisse, 2014). 4

Figure 1.4. The general structure of Ultrasound and MRI imaging systems. (A) Ultrasound system. (B) MRI system (Izadifar, Izadifar, Chapman, & Babyn, 2020). 5
Figure 1.5. Mini opto tomography platform. (A) Geometric structure. (B) Ray diagram. (C) Mechanical structure (Polat et al., 2019). 7
Figure 1.6. General structure of digital breast tomosynthesis. DBT creates a new 3D image by using images obtained from different angles (Helvie, 2010). 8
Figure 1.7. Production of MCF-7 spheres of different sizes, whose diameter was determined after 3 days of culture. (A) Spheroids of different diameters. The spheroid radius of each group are equal in themselves. (B) Spheroid size can be controlled by varying numbe. 9
Figure 1.8. Scaling the sample by applying a microscopic imaging technique to the biological sample (Emmert-Streib & Dehmer, 2015). 9
Figure 3.1. (A) First, 10th and 40th layers of 3D images reconstructed on Day 4. (B) 3D image with different perspectives consisting of 50 layers (Polat et al., 2019). 13
Figure 3.2. Cancer images that with contours are drawn manually. (A) Day 2 layers. (B) Day 4 layers. (C) Day 6 layers (Polat et al., 2019). 14
Figure 3.3. The block diagram of the image processing system applied to images used in the study. 15
Figure 3.4. Steps to reach the second, fourth and sixth day layers with ImageJ program. 16
Figure 3.5. Second, fourth and sixth day layers. (A) Second day layers. (B) Fourth day layers. (C) Sixth day layers (Polat et al., 2019). 17
Figure 3.6. (A) Gri scale image. (B) RGB colored image (Kumar & Verma, 2010). 18
Figure 3.7. Display of filtering process (Lyra et al., 2011). 20
Figure 3.8. The result images and matrix values when the mean filter is applied to the input image. 21
Figure 3.9. Change of the center pixel value in the area covered by the core matrix when a median filter is applied to the input image (Boateng et al., 2012). 22
Figure 3.10. Result images and matrix values when a median filter is applied to the input image. 23
Figure 3.11. Structure of bilateral filter with spatial filter and range filter (Porikli, 2008). ... 24
Figure 3.12. When the different size of the Gaussian filter is applied to the original image, the result images and the binary images obtained from the result images. 25
Figure 3.13. Image graphic divided into two parts according to the selected x value (Rogowska

& analysis, 2000). 27
Figure 3.14. Threshold view of rice grains. After the thresholding process, the rice grains became the object and the black sections became the background (McAndrew & Mathematics, 2004). 28
Figure 3.15. Application of adaptive thresholding method. (A) Original image. (B) Simple thresholding result. (C) Image fragmentation. (D) Adaptive thresholding result (McAndrew & Mathematics, 2004). 29
Figure 3.16. Application of the Otsu's thresholding method on original noisy and gaussian noisy images (Mordvintsev & Abid, 2017). 30
Figure 3.17. Results of the thresholding methods applied to the spheroid image. (A) Original image. (B) Global thresholding result. (C) Adaptive thresholding result. (D) Otsu’s binarization result. 31
Figure 3.18. Expansion of the input image as a result of using structural elements (Raid et al., 2014). 32
Figure 3.19. Eroding of the input image as a result of using 3x3 structural element (Acar & Bayram). 33
Figure 3.20. Representation of opening and closing processes (Raid et al., 2014) 33
Figure 3.21. Applying morphological operations which are called erosion and dilation to the original image, respectively, and obtaining the output image. 34
Figure 3.22. Applying morphological operations which are called dilation and closing to the original image, separately and obtaining the output image. 34
Figure 3.23. Effect of contour approach method on images (Mordvintsev & Abid, 2017). ... 35
Figure 3.24. Drawing the contour boundary for the main tumor mass. A) Original image. B) Binary image obtained after thresholding. C) Applying erosion to the binary image. D) More than one contour drawing. E) Automatic plotting of the boundary line for the main tumor mass. 36
Figure 3.25. A) Original image. B) Applying edge detection to the original image. C) Applying edge detection to noisy+binary image. D) Applying edge detection to noiseless + binary image. 37

Figure 3.26. The geometrical feature extraction of cancerous images. A) Original image. B) Contour perimeter in pixel. Perimeter is the sum of the pixels of the contour boundaries. C) Contour area. The contour area is the sum of the pixels within the boundaries surrounding the main tumor mass. D) Circle radius. The circle radius is the radius of the circle that minimally surrounds the main tumor mass. 39

Figure 4.1. For the images belonging to the second, fourth, and sixth days, the main tumor masses that the contour boundaries are automatically drawn. 40

Figure 4.2. Total area values in pixels for the second, fourth and sixth days. 42

Figure 4.3. Area values of main tumor masses belonging to the layers of spheroid structures on the second, fourth, and sixth days. 42

Figure 4.4. Perimeter growth values of main tumor masses belonging to the layers of spheroid structures on the second, fourth, and sixth days. 43

Figure 4.5. Radius values for the circles surrounding as minimum the main tumor structures that belong to the second, fourth, and sixth days. 45

LIST OF TABLES

Table 3.1. CNR values obtained as a result of filters applied to the second, fourth and sixth day images. 26

Table 4.1. Area values of main tumor structures of the second, fourth, and sixth days in pixels. 41

Table 4.2. Perimeter values in pixels of main tumor structures on the second, fourth, and sixth days. 43

Table 4.3. Radius values in pixels of main masses on the second, fourth, and sixth days. 44

NOMENCLATURE

ART	: Algebraic Reconstruction Technique
BPPN	: Back Propagation Neural Network
BEMD	: Bidimensional Empirical Mode
CAD	: Computer-Aided Diagnosing
CLAHE	: Contrast Limited Adaptive Histogram Equalization
CNR	: Contrast To Noise Ratio
CT	: Computed Tomography
DBT	: Digital Breast Tomosynthesis
GUI	: Graphical User Interface
MOTP	: Mini Opto Tomography Platform
MRI	: Magnetic Resonance Imaging
OpenCV	: Open Source Computer Vision Library
PSNR	: Peak Signal to Noise Ratio
RBFN	: Radial Basis Neural Networks
RMSE	: Root Meam Square Error
SART	: Simultaneously Algebraic Reconstruction Technique
SIRT	: Simultaneous Iterative Reconstruction Technique
2D	: 2-Dimensional
3D	: 3-Dimensional

1. INTRODUCTION

Cancer is the name of a group disease formed by uncontrolled growth and spread of cells in certain parts of the body (Çığır, 2011). Thousands of people die every year due to cancer in the World. According to the American cancer society, 1,806,590 cancer cases will be detected and 606.520 cancer deaths will occur in the United States in 2020 (Siegel, Miller, & Jemal, 2020). Figure 1.1 shows the estimated number of diagnoses and mortality rates for the most common types of cancer in men and women in the U.S. in 2019 (Siegel, Miller, & Jemal, 2019).

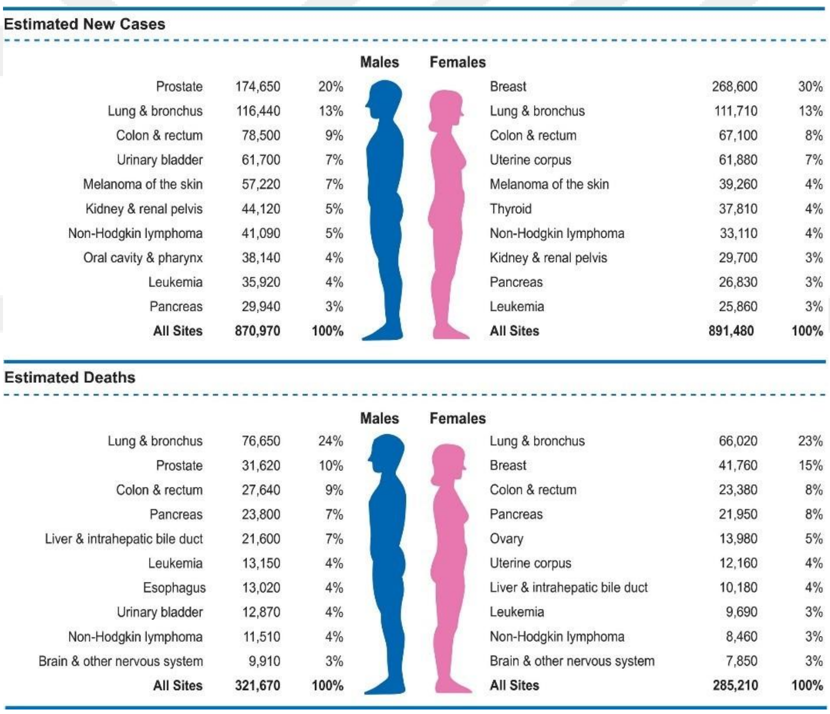

Figure 1.1. The estimated cancer types and mortality rates by gender in United States, in 2019.

When Figure 1.1 is examined, prostate, lung and colon cancer types make up 42% of the cancer types expected to be seen in men. In women, breast, lung and colon cancers are the most common types of cancers expected to be seen.

1.1. Breast Cancer

Breast cancer stands out alone as the highest cancer rate in women. Breast cancer death rates have prevented between 384.000 and 614.500 together with increased mammography scanning and improved treatment, by falling between 1.8% and 3.4% per year in the United States since 1990 (Hendrick, Baker, & Helvie, 2019). Figure 1.2 shows the mortality rates due to breast cancer for women at the age of 40-84 from 1969 to 2019. In the figure, it is seen that the death rates for each woman have decreased linearly from 2016 to 2019 (Hendrick et al., 2019).

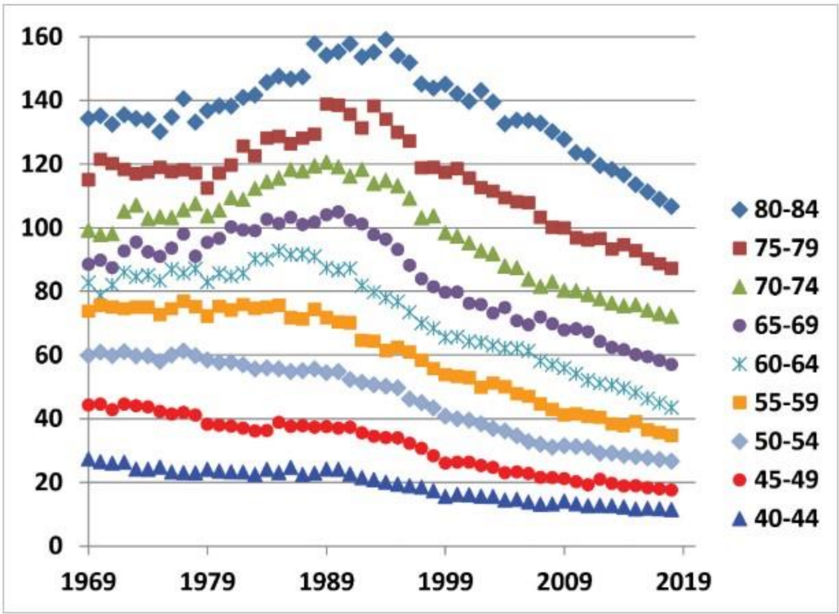

Figure 1.2. The death rates due to breast cancer in women between the ages of 40-84 in the USA from 1969 to 2019 (Hendrick et al., 2019).

Breast cancer cells are divided into two groups as benign and malignant. The benign cancerous cells are the normal ones that grow slowly and don't spread to other organs in the body. Malignant cancerous cells are aggressive cells and these cells spread from the regions where they are located to other parts of the body (Makandar & Halalli, 2015). If the malignant cancer cells are not treated on time, these cells can be fatal to the patient. Therefore, early diagnosis and the right treatment method is vital for the patient to hold on to life.

1.2. Breast Cancer Imaging Methods

The goal of imaging methods used to display the breast cancer cells is to detect the cancerous cells at an early stage and to ensure that the patient to hold to life. Cancer imaging methods are very important for specialists to read accurately on cancerous cells and develop effective treatment methods.

1.2.1. Mammography

Mammography is a special type of imaging for scanning and diagnosing human breast using low energy X-rays (Polat, 2018). In mammography, which is the most common screening method for breast cancer, it is possible to detect cells that are too small to be felt (Screening & Board, 2020). Standard mammograms take two views of each breast, horizontal and vertical, while 3D mammography, also known as digital breast tomosynthesis, creates a new 3D image by reconstruction of images taken from different angles of the breast (Helvie, 2010). 3D imaging provides a more detailed and clearer image than traditional 2D imaging.

Because cancer disease is a combination of many diseases, mammography images are not sufficient to detect cancer alone (Cahoon, Sutton, & Bezdek, 2000). Thus, the application of various computer-aided methods to mammography images has been an important factor in the detection and interpretation of cancer.

Although mammograpy is the most effective scanning method for breast cancer detection, it has some disadvantages. Especially, as young women has more texture density, it will be difficult to detect cancer which is in breast in this structure. Therefore, additional imaging methods like digital breast tomosynthesis (DBT), magnetic rezonans imaging (MRI), ultrasound are some of the methods used to support mammograpy in early detection (Hooley, Andrejeva, & Scoutt, 2011).

1.2.2. Digital Breast Tomosynthesis

In the digital breast tomosynthesis (DBT) imaging method, which is a new generation imaging method, a 3-dimensional image of the breast is created using X-rays moving at a limited angle for the breast organ. In other words, a new 3-dimensional image is created by reconstructing two-dimensional images obtained from different angles in the DBT method (Seyyedi, Cengiz, Kamasak, & Yildirim, 2013). Figure 1.3 shows the general structure of the digital breast tomosynthesis system.

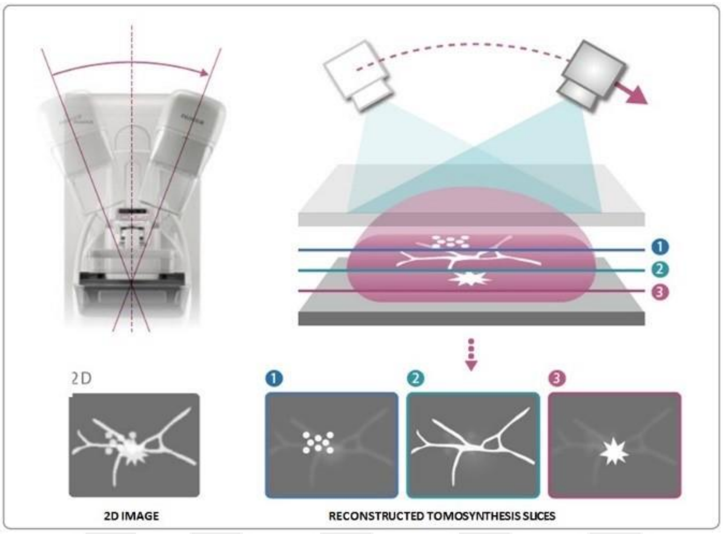

Figure 1.3. General structure of digital breast tomosynthesis (Schulze-Hagen, Eshghi, Müller, & Müller-Leisse, 2014).

1.2.3. Ultrasound

Ultrasound that can be used to detect regions where the suspicious lesions are located directs high-frequency sound waves to breast textures and creates 2D images by detecting reflected sound waves (Sree, Ng, Acharya, & Faust, 2011). The general structure of ultrasound imaging is shown in Figure in 1.4a.

1.2.4. Magnetic Resonance Imaging

Magnetic resonance imaging (MRI) method is commonly used to take high-resolution images in women with dense breasts who are at high risk of breast cancer. Also, since there is no radiation, the MRI method has no side effects. The MRI method has some disadvantages in some cases. This method does not show all the calcifications in the breast, it is slow and expensive (Sree et al., 2011). The MRI system is shown in Figure 1.4b.

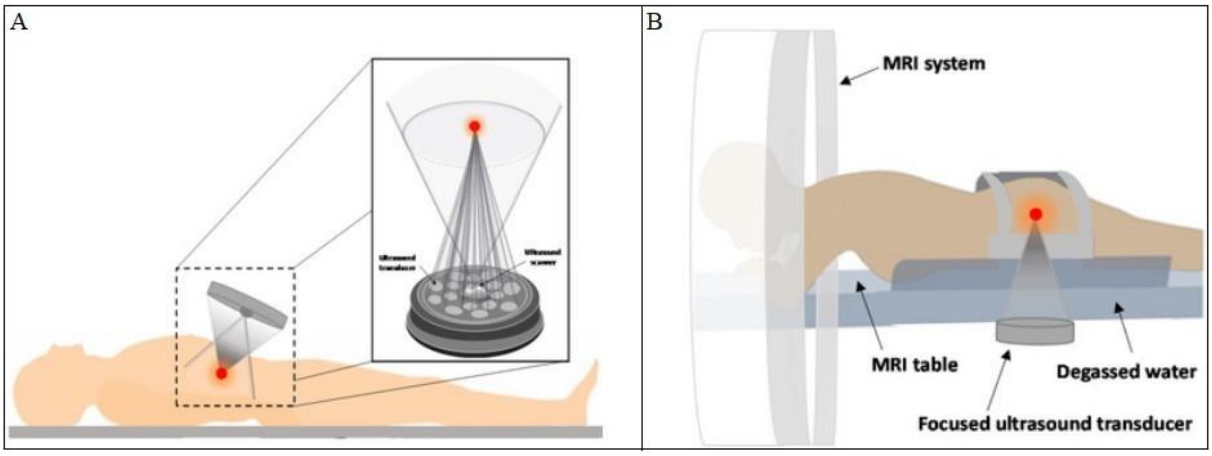

Figure 1.4. The general structure of Ultrasound and MRI imaging systems. (A) Ultrasound system. (B) MRI system (Izadifar, Izadifar, Chapman, & Babyn, 2020).

1.3. Scope of The Thesis

In this thesis study, the main tumor masses in the images containing cancer cells were detected in their development environment using computer-aided image processing systems. In addition, in order to examine the development of three-dimensional breast cancer cells on the second, fourth and sixth days, the changes of the two-dimensional layer images in terms of perimeter radius and area were calculated. While color transformation, filtering processes were applied to improve the images in the pre-processing stage, thresholding, morphological processes, and contour extraction processes were applied in the segmentation stage. Finally, in the feature extraction step, the perimeter, radius, and area values of the main tumor masses in the images were calculated. In the conclusion part, these mathematical values were compared and the growth developments of the main tumor masses on 3 different days were examined by considering the perimeter, radius, and area values.

The images used in the study were the layers on the second, fourth, and sixth days of the 3dimensional cancerous image formed by cells named MCF-7. With the Mini-Opto tomography platform, a new 3D image was created using various reconstruction techniques for the cancerous structure, whose images were taken from different angles. Below, computer-aided image processing system, the mini-Opto device, algebraic reconstruction technique, MCF-7 cells, and light microscope are explained in more detail.

1.3.1. Computer-Aided Image Processing Systems

With technological advances, obtaining better quality images and developing computer systems has improved the interpretation of medical images, and has greatly contributed to early diagnosis (Stoitsis et al., 2006). Image pre-processing, segmentation, feature extraction, and classification constitute the main structure of a computer-aided image processing system. In the preprocessing step, noisy areas are tried to be reduced as much as possible with noise reduction and filtering processes. While the purpose of the segmentation step is to determine some objects and borders in the image, the important features in the image are extracted with the feature extraction process and thus the image is analyzed in detail.

Python programming language and OpenCV library were used as a computer-aided image processing system in the thesis study. Python is an object-oriented, interpretative, and interactive high-level programming language that enables fast improvements with a simple syntax designed by Guido van Rossum in 1990 (Sanner, 1999). The OpenCV library is an opensource library created with a group of C /C ++ functions and classes that allows real-time applications to be developed, used to achieve powerful image processing, and offers a wide variety of libraries (Xie, Lu, & Engineering, 2013).

1.3.2. Mini Opto Tomograpy Platform

Mini-Opto tomography platform is an electronic, mechanic, and software-based platform that can display cancer cells in 3D (Polat et al., 2019). In my thesis, the images obtained with different angles from the mini-Opto tomography platform were used to observe the volumetric changes of main tumor masses within the images at certain time intervals. Mini-Opto tomography platform that can monitor cancerous cells as 3D and creates a 3D image by reconstructing images obtained from different angles is a combined version of digital breast tomosynthesis used in angular scanning and optical-based microscopy technology. Figure 1.5 shows the geometric and mechanical structure of mini-Opto tomography platform. The mechanical body is the structure that carries all the optical components, electronic parts, and organ models. With the mini-Opto tomography device, it can be monitored volumetrically how the given drug treatments affect to minimize or destroy a tumor over time. By developing this device further, it is possible to create a 3D image in high resolution. At the same time, the system of the electronic card-assisted mechanical design will enable more images to be taken from different angles in a short time for reconstruction (Polat et al., 2019).

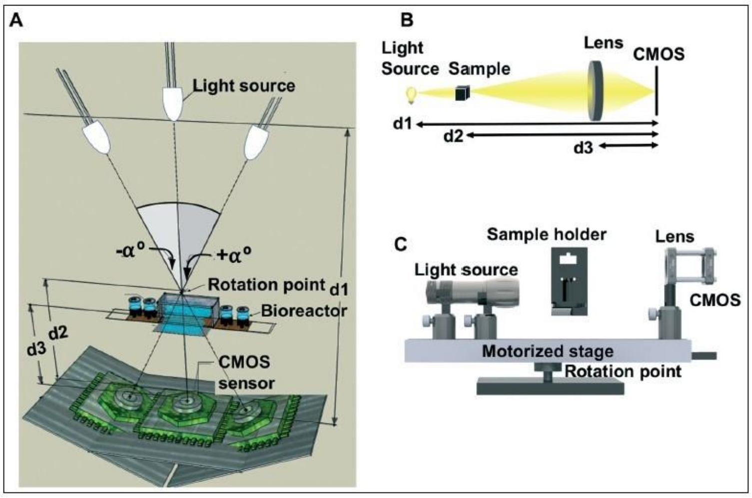

Figure 1.5. Mini opto tomography platform. (A) Geometric structure. (B) Ray diagram. (C) Mechanical structure (Polat et al., 2019).

1.3.3. Algebric Reconstruction Technique

There are many reconstruction technique to reconstruct the image using the image projections. Some of reconstruction techniques are algebraic reconstruction technique (ART), simultaneously algebraic reconstruction technique (SART), simultaneous iterative reconstruction technique (SIRT).

The reconstruction technique used in the creation of 3D images is Algebraic Reconstruction Technique (ART) which is an algebraic reconstruction technique which is an emerging method to create a new 3D image from images taken from digital breast tomosynthesis to display suspicious lesions (Polat, Yildirim, & Technology, 2018). The main purpose of ART methods is to make 3D imaging in high resolution, at lower dose levels, and fewer noise levels. Because, while obtaining the 3D image of the breast with DBT, X-rays taken from different angles are used. While crossing the X-rays through the breast, the intersection lengths and indices are calculated and the image is created. It is important for the patient's health that the dose level is minimum while the image is created (Polat et al., 2018).

Looking at Figure at 1.6, a clamping plate compresses the breast and X-ray Tube scans the breast with a limited view angle of 11 ° -60 °. As this limited angle scan in DBT causes missing data set problems, advanced reconstruction techniques are used to prevent this problem (Polat et al., 2018).

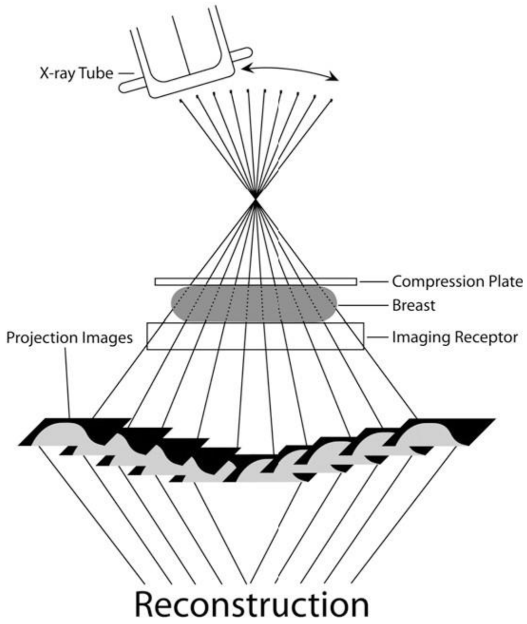

Figure 1.6. General structure of digital breast tomosynthesis. DBT creates a new 3D image by using images obtained from different angles (Helvie, 2010).

1.3.4. MCF-7 Cells

MCF-7 cells which are derived from a woman with metastatic breast cancer treated with radiation therapy and hormone manipulation at the Michigan Cancer Foundation before is a breast cancer cell line that is widely used in breast cancer studies (Osborne, Hobbs, Trent, & treatment, 1987). Cells express receptors and biological responses for various hormones, including estrogen, androgen, progesterone, glucocorticoids, insulin, epidermal growth factor, insulin growth factor, prolactin, and thyroid hormone (Osborne et al., 1987).

1.3.5. Light Microscopy

Since its invention in the 17th century, light microscopy have been an important structure to make analyzes and determinations on cell biology studies (Polat et al., 2019). In addition, many cells have been discovered in biology and medicine with the discovery of the conventional microscope. Various imaging methods such as MRI and X-rays have been developed inspired by microscope technology (Emmert-Streib & Dehmer, 2015). Although conventional light microscopy has contributed significantly to scientific research since it is discovered, it has a significant deficiency in the 3D imaging point on cells. As seen in Figure 1.8, a conventional light microscope magnifies tens of times the biological cells that will not be visible and it bring them to the level that the human eye can see.

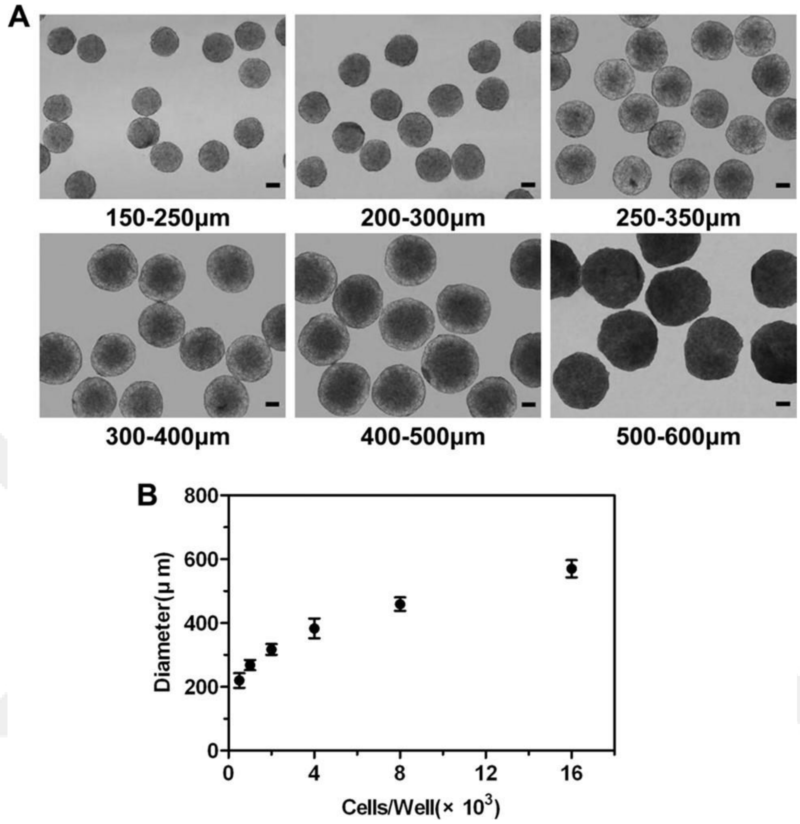

Figure 1.7. Production of MCF-7 spheres of different sizes, whose diameter was determined after 3 days of culture. (A) Spheroids of different diameters. The spheroid radius of each group are equal in themselves. (B) Spheroid size can be controlled by varying numbe.

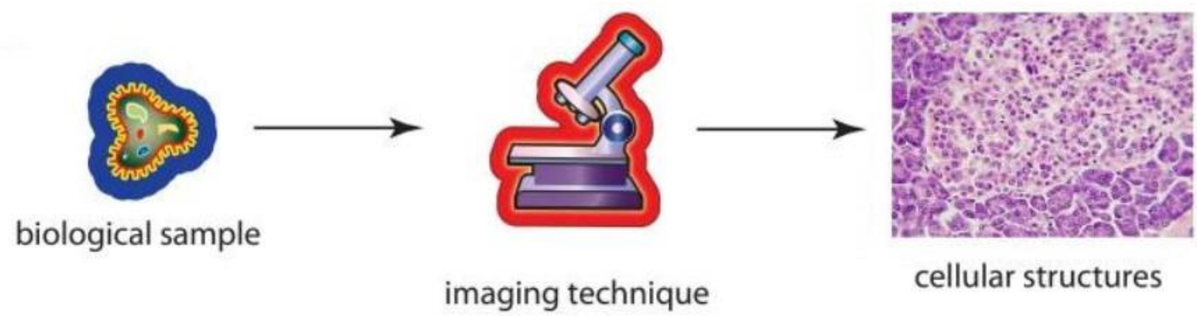

Figure 1.8. Scaling the sample by applying a microscopic imaging technique to the biological sample (Emmert-Streib & Dehmer, 2015).

2. LITERATURE REVIEW

There are many articles and studies in the literature on the detection of breast cancer cells and the observation of their growth developments. Scientific studies and technological developments have made important contributions to the detection and development of breast cancer cells. Computer-aided image processing systems that perform many operations such as reading, preprocessing, and segmentation on cancerous images are of vital importance for radiologists to make accurate analyzes on images. After being obtained cancerous images, correct implementation of image processing methods on these images will increase the reliability of the results to be obtained. In my thesis, I applied computer-aided image processing methods on spheroid images formed by breast cancer cells called MCF-7 developed in the laboratory environment. Scientific studies in the literature related to my work are listed below.

The images we use in our study are 3-dimensional images consisting of the combination of dozens of layers obtained from mini opto tomography platform developed by Polat et al. It is possible to display cancerous cells as 3-dimensional with the mini-Opto tomography platform. Actually, breast cancer cells can be displayed in 3D with digital breast tomosynthesis or similar devices. Although the cost of these devices is quite high, the mini-Opto tomography platform is very advantageous in terms of low cost. A new 3D image creation process on the mini-Opto tomography platform is made by reconstructing images obtained in a certain amount from different angles. It is possible to monitor as volumetric how much it will affect the tumor of given drug treatments to shrink or eliminate a tumor over time with this device. By being improved this device further, it can be created a 3D image in high resolution (Polat et al., 2019).

Alhadidi et al. made a study showing how cancer to be diagnosed using a threshold, edge-based, watershed segmentation methods in a breast image obtained from the mammogram. Also, in this study, there are comparisons in terms of time and simplicity among the methods used in cancer detection. Altough the threshold method gave the fastest result in the study, the image obtained by the threshold method gave a worse segmentation result than the other methods. In addition, it was concluded that watershed segmentation takes more time than the threshold but it gives a better quality image (Alhadidi, Zu'bi, & Suleiman, 2007).

Kamini and Yadav aimed to detect breast cancer using the “Bidimensional Empirical Mode Decomposition (BEMD)” method. This study consists of two parts: the first is to find suspicious masses in mammography and the second is to find the contours of these masses. It was seen that the BEMD technique played an important role in developing computer-aided diagnosis quality (Waghulade & Yadav, 2016).

Sharma and Jindal developed an automatic CAD (Computer-Aided Diagnosis) system to detect lung cancer. In the study, 1000 lung images were taken from the NIH/NCI union which contains a database of lung images. The images were introduced to the system used in the study. Later, when an image was entered the system, it was determined whether there was cancer in the image. In the experiments made at end of the study, it was concluded that the system has achieved great success in detecting cancer with high sensitivity (Sharma & Jindal, 2011).

In 2013, Kaushik et al. discussed different aspects of automatic image segmentation for medical images. They stated that image segmentation is affected by many factors such as image homogeneity, spatial properties of image, image content. Therefore, it was said that the image processing methods don’t always provide satisfactory results for segmentation. So, they concluded that image segmentation remains a challenging problem in image processing and computer vision (Kaushik, Singh, Singhal, & Singh, 2013).

At the study done in 2015 by Barole et al. they compared techniques such as MRI, CT scan, ultrasound, and ray for medical imaging. In this study, it was stated that the MRI technique is the most suitable method for brain tumor detection. Also, the importance of various digital image processing techniques for brain tumor detection was emphasized. In addition, it was stated that methods such as threshold, histogram, morphological operations are used to improve the images (Borole, Nimbhore, Kawthekar, & Science, 2015).

Joseph et al. performed a classification process on MRI images. In the study, the K-Means Clustering method was used as an unsupervised classification technique which automatically classifies objects according to the criteria given by the user. Tumor MR Images were taken to use the proposed algorithm according to the simulation results and the GUI window was designed to make the process better. After brain MR images were collected from the database, these images were clustered, and eventually, the tumor was brought fore by applying morphological operations (Joseph, Singh, Manikandan, & Technology, 2014).

Makandar and Halalli performed noise removal and contrast enhancement operations on mammography images. Many noise removal methods such as average, min-max, Wiener, median are used to reduce the noise level. Quality measurements such as RMSE and PSNR were used to analyze filtering techniques and Wiener filter gave minimum RMSE values and maximum PSNR values. In the study, it was concluded that the Wiener filter method is most proper for reducing the image noise. In addition, it was stated that Contrast Limited Adaptive Histogram Equalization (CLAHE) algorithm is the best method to increase the contrast of the image (Makandar & Halalli, 2015).

Kaymak et al. proposed an automatic image classification method for breast cancer in their study. In the study, the classification of images was performed using Back Propagation Neural Network (BPNN) and radial basis neural networks (RBFN). The accuracy of BPNN and RBFN was measured as 59% and 70.4%. Both networks were made on the same training images and the same test images. The results showed that RBFN performs better than BPNN (Kaymak, Helwan, & Uzun, 2017).

Primkhajeepong et al. presented an automatic algorithm to analyze automatically of breast cancer cell image. The developed automatic algorithm was compared with a specialist view. The advantages of the proposed method over traditional methods are automatic counting of cancer cells and comparison of their performance with the result obtained by a pathologist (Primkhajeepong et al., 2010).

3. MATERIALS AND METHODS

The images of 3D layered breast cancer cells called MCF-7 produced in the Lab-on-a-chip environment were used in the study. 3D layered images were obtained using a mini-Opto tomography platform which is used to create a new 3D image for cells obtained from different angles (Polat et al., 2019). The number of images obtained on the 2nd, 4th, ve 6th days of the spheroid structure formed by MCF-7 cells is 150.

Each layer in the 3D image created by ART (Algebraic reconstruction technique) was obtained with the ImageJ. As the images of cancer cells in successive layers are close to each other, only 10 of the 50 layers obtained for every day were used. Figure 3.1 shows the images of the first, tenth, and fortieth layers obtained on the fourth day and three-dimensional volumetric images formed by cancer cells.

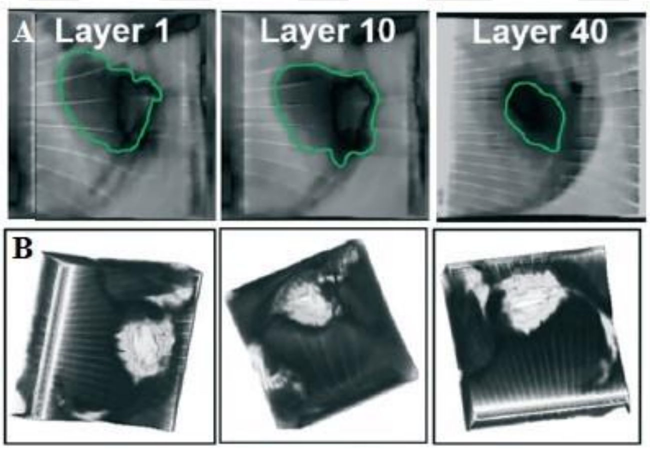

Figure 3.1. (A) First, 10th and 40th layers of 3D images reconstructed on Day 4. (B) 3D image with different perspectives consisting of 50 layers (Polat et al., 2019).

For each day, 5, 10, 15, 20, 25, 30, 35, 40, 45 ve 50th layers in 200x200 pixel size of the 3D raw image with .ima format reconstructed were obtained using ImageJ program. Figure 3.2, when examined carefully, a dark black region in each layer within the spheroid represents the main cancerous cells. Approximately contours of main tumor masse were drawn manually using ImageJ by Polat et al. in 2019. After tumor contours were drawn manually, it was observed that the volumetric changes of tumors increased from the 2nd day to the 4th day and from the 4th day to the 6th day.

For example, in Figure 3.2, looking at the 25th layers of 2nd, 4th, and 6th days, it is seen that the volumetric and area changes of tumors are evident. Although objects with shades similar to cancerous cell colors at the edges of spheroids are similar to cancerous cells called MCF-7, these structures are not included in the contour border areas. When the contours of cancerous structures are drawn automatically, these structures are not included in the automatic drawing. The aim is to reach the main tumor structure.

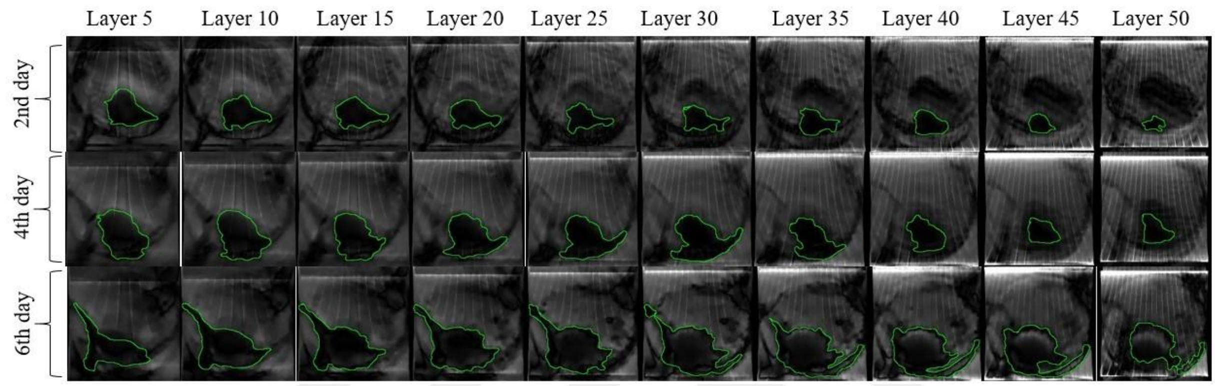

Figure 3.2. Cancer images that with contours are drawn manually. (A) Day 2 layers. (B) Day 4 layers. (C) Day 6 layers (Polat et al., 2019).

In the thesis study, computer-aided image processing techniques were applied to the images to detect the main tumoroid structure formed by MCF-7 cells in a bioreactor, to draw the boundaries, and to calculate the growth developments. Image processing includes the methods that the image starts with a gray or colored pixel array and ends with another image (Russ, 1990). After applying image processing methods on an image, there may be changes in the properties of the image such as size and color.

As the computer-aided image processing systems on the images, the open-source Python programming language and OpenCV (Open Source Computer Vision Library) environment which has many libraries were used. The open-source OpenCV library which is accessible freely for everyone has been developed by Intel and it is used at many Computer Vision applications today. OpenCV library which was was designed taking into account computing efficiency and real-time applications has been coded using C/C++ programming languages (Mohamad, Saman, Hitam, & Telipot, 2015).

The image processing methods used on the images to identify the cancerous structure and to observe their growth development are discussed under 4 main titles. Figure 3.3 shows the block diagram of the image processing system.

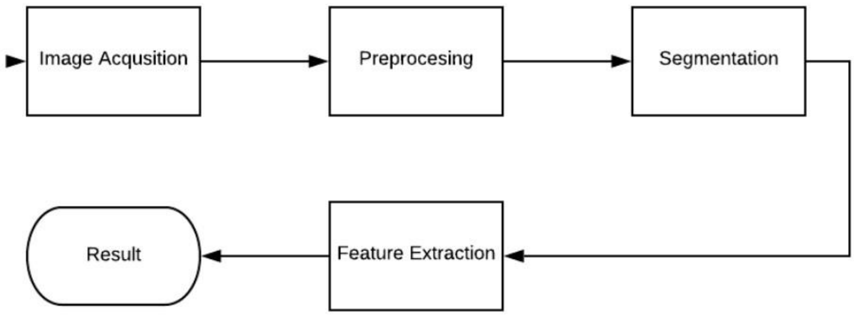

Figure 3.3. The block diagram of the image processing system applied to images used in the study.

If we briefly mention the main titles of the image processing system in Figure 3.3, image acquisition is the case of converting images into a suitable format. In the preprocessing step, the unnecessary objects in the images are eliminated and the quality of the images are improved. The segmentation is to distinguish the objects from the background, that is, grouping the pixels of the respective regions. Feature extraction is the operation of removing important features of the segmented images.

3.1. Image Acqusition

In the study, the ImageJ program was used to obtain layered images. With the ImageJ program, it is possible to reach layers of 3D images that have been reconstructed with .ima extension. ImageJ is a java image processing and analysis program with open source coded. In addition, it is possible to edit 8-bit, 16-bit, 32-bit images with ImageJ and this program supports images in TIFF, GIF, JPEG, BMP, DICOM, FITS, raw formats (Ferreira & Rasband, 2012). It is possible to calculate area and pixel values using the ImageJ program which supports standard image processing functions such as image smoothing, edge detection, and median filtering (Ferreira & Rasband, 2012). In our study, the processes were performed on images with .ima extension and raw format. After the 3D images formed using ART + TV_{3D} reconstruction technique were separated into layers, these images were saved as .ima extension for the 2nd, 4th, and 6th days.

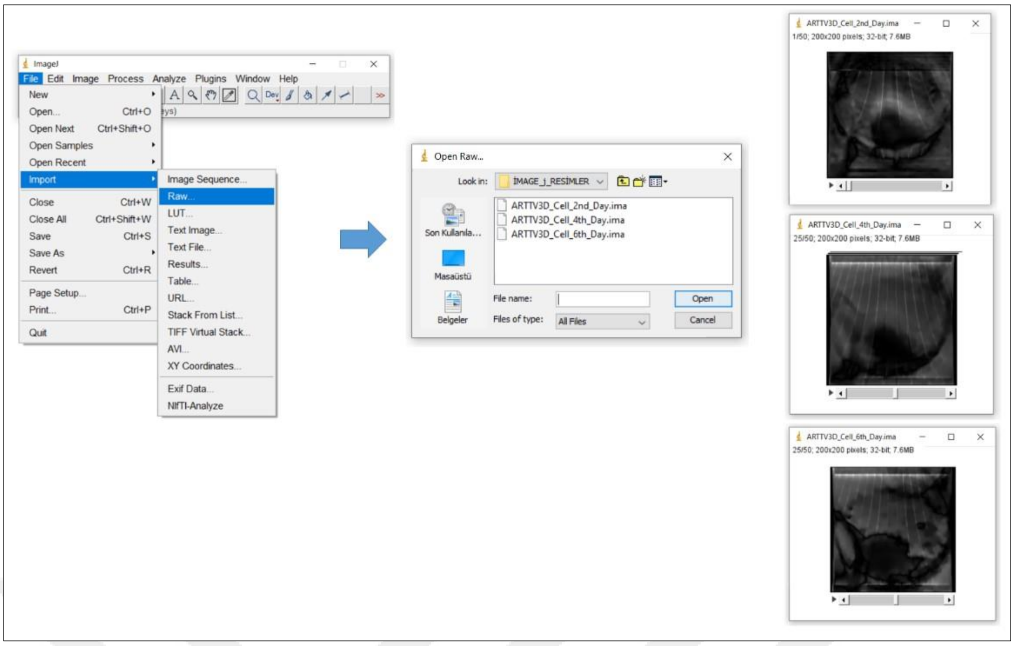

Figure 3.4. Steps to reach the second, fourth and sixth day layers with ImageJ program.

When looking at Figure 3.4, in order to reach the layers of the spheroid structure, when importraw is selected in the ImageJ program, the file containing the raw data with the .ima extension was opened. Then, whatever layers of the day are desired to be reached, the raw data file belonging to that day was selected and the data with the .ima extension was reached. There are 50 layers in each file with .ima extension, and we worked on 10 layers per day. It was done necessary processes on 10 layers belonging to Figure 3.5A when .ima file of the 2nd day is selected, to Figure 3.5B when the .ima file of the 4th day is selected and to Figure 3.5C when the .ima file of the 6th day is selected.

3.2. Preprocessing

In an image processing application, the purpose of the preprocessing step is to increase the image quality, that is, to enhance the image. In the preprocessing stage, the image is made ready for the segmentation step (Yildiz, Demir, & Ülkü, 2017). In our study, during the image preprocessing stage, the images are converted to gray format, and filtering processes are performed on the image, respectively.

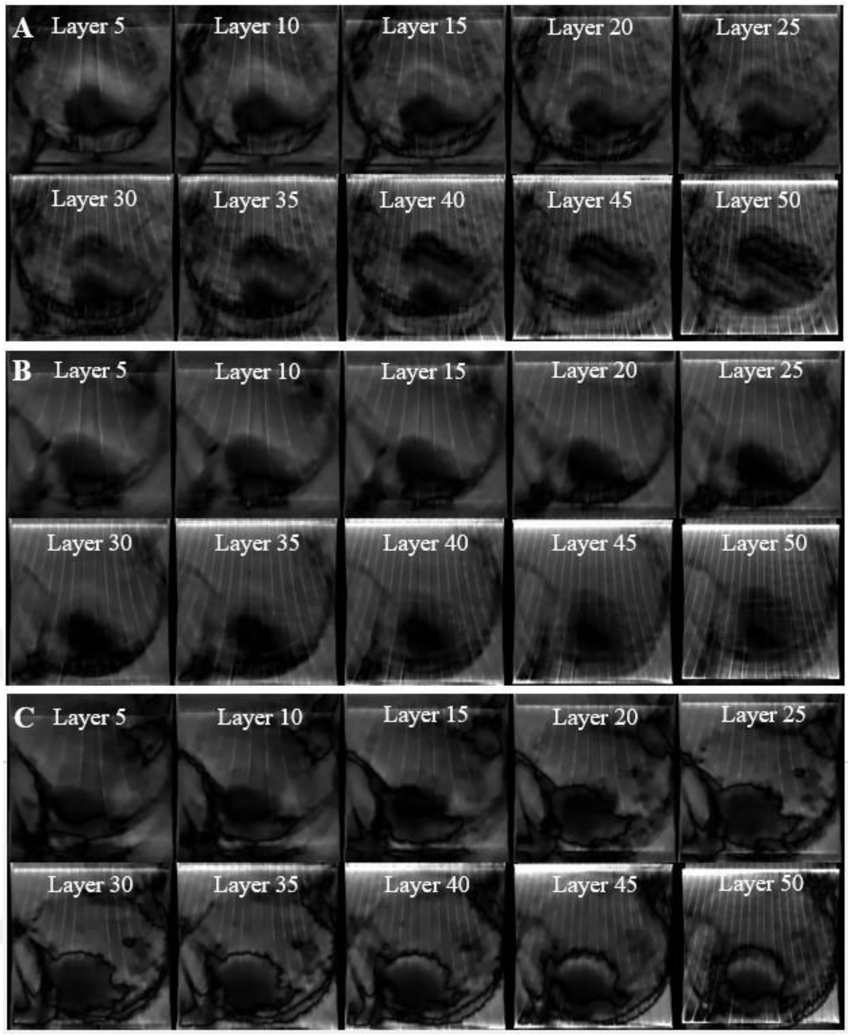

Figure 3.5. Second, fourth and sixth day layers. (A) Second day layers. (B) Fourth day layers. (C) Sixth day layers (Polat et al., 2019).

3.2.1. RGB to GRAY Transformation

In the process of converting from RGB to Gray, RGB toned images were converted to gray intensity images. In the RGB color model, the value of a pixel consists of three main components corresponding to the color intensities of Red, Green, and Blue. A color image in this color model is expressed by the density function in equation 1 (Kumar & Verma, 2010).

$I_{RGB} = (F_R, F_{G,} F_B)$ (1) $F_R(x, y)$ is the intensity of (x,y) pixel in red color, $F_G(x, y)$ is the intensity of (x,y) pixel in green color and $F_B(x, y)$ is the intensity of (x,y) pixel in blue color (Kumar & Verma, 2010). The intensity of each color channel is usually stored as 8-bit and so, a colored pixel stores a 24-bit data. 24-bit data have value between 0 and 256x256x254=16774216. Figure 3.6B shows the RGB color image.

In gray level images, every pixel value carries only gray tones intensity information and the contrast in grayscale images is between the color changing from the weakest intensity black to the strongest intensity white (Johnson, 2006). There are $2^8 = 256$ gray levels in an 8-bit graylevel image. So the density of each pixel can be between 0 and 255. A value of 0 represents black, and a value of 255 represents white. Another commonly used storage method is 1-bit storage. In this storage method, 0 represents black and 1 represents white. This image format, which is frequently used in medical imaging, is called a binary image (Kumar & Verma, 2010). Figure 3.6A shows the gray density image.

Figure 3.6. (A) Gri scale image. (B) RGB colored image (Kumar & Verma, 2010).

In the study, first, the images in RGB format were converted to gray color intensity. For the next steps after this process, gray density images were used for the image processes steps which consist of pre-processing, segmentation, feature extraction. Because gray-level images are completely sufficient for many tasks and so it doesn't need to use colored images that are more complex and difficult to be processed. As seen in the equation below, the gray-colored image was obtained by multiplying W weight values by R, G, B color values (Yildiz et al., 2017).

$$Gray_{image} = W_R x R + W_G x G + W_B x B \quad (2)$$

It is necessary to be found of conversion weights to obtain gray-level images. After the conversion weights are found, the color value of each weight is multiplied by weights and the output image is obtained.

3.2.2. Image Filtering

While applying image processing techniques on an image, one of the important steps is image filtering. The blurred and noise on an image cause to decrease in image quality and it will be difficult to process the image. Mathematical operations are applied to the image to remove noise on the image and increase the resolution of the image. After applying these mathematical operations, the resolution of the image may increase and the distortions on the images may remove (Lyra, Ploussi, Georgantzoglou, & Ionescu, 2011). In fact, by filtering operations, some details in the image may come to the foreground or suppress.

In image filtering, the distinction between the physical properties of the image increases, making it easier to interpret the image. The mathematically applied process on images to filter the image is to combine various filtering matrices with the image. Different filtering processes are applied to increase the image resolution, smooth the boundary lines, or reduce the noise in pre-processing step (Altuntaş & Çorumluoğlu, 2011). In the filtering process, matrices arrays in different sizes such as (3x3, 5x5, 6x6) are selected to apply to the input image. This matrice is named as a kernel and the kernel size changes according to the filtering method to be applied. During filtering, the kernel is moved over all pixels on the image and so, the output image is obtained. Figure 3.7 shows an example filtering process.

Before looking filter method we applied on cancerous cells called MCF-7, it is mentioned about filter methods used frequently in the OpenCV environment such as mean, median, gaussian, and bilateral below.

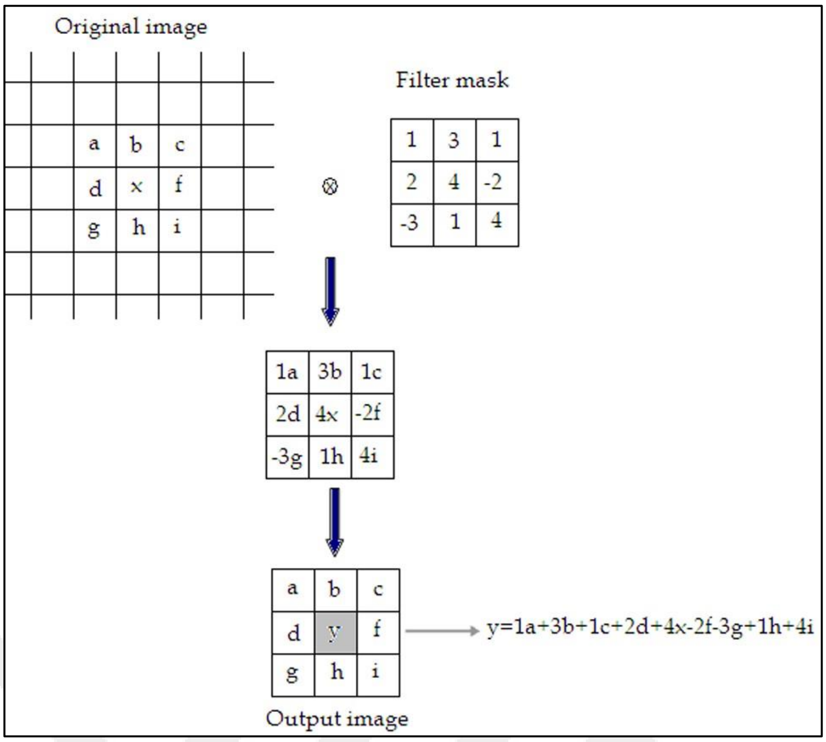

Figure 3.7. Display of filtering process (Lyra et al., 2011).

3.2.2.1. Mean Filter

The mean filter is the simplest low pass filter in which, each pixel value is replaced by the average value created by the neighboring pixels and itself. Thus, pixel values that don't represent its environment are eliminated. The mean filter can also be called an average filter which is a simple and easy-to-apply method of smoothing images. In other words, the purpose of the mean filter is to reduce the amount of change between one pixel and the surrounding pixels (Lyra et al., 2011). This filter which is called a convolution filter is often used to reduce noise in images. In the convolution process, the pixels on the images are multiplied and shifted and so, the smoothing value on the image is increased or decreased by kernel matrice that is applied to input image. The mathematical representation of the value y (i, j) is shown as follows if we express as y (i, j) the output image that will occur as a result of applying the filter function of f (i, j) to an input image of x (i, j).

$y(i,j) = f(i,j) \odot x(i,j)$ (3) When the mean filter is applied to 2nd-day and layer-5 with different kernel values, the result images are shown in Figure 3.8. Figure 3.8, when examined carefully, it is seen that when the kernel in size (3x3) is applied to input image, the output image becomes soft. Also, when the matrix values of the output image are examined, it is seen that the values are close to each other. When the mean filter process with dimensions of 10x10 is applied to the input image, it is seen that the softening in the output picture is more. Considering the matrix values of the final image, the values in the same region are closer to each other. When the mean filter value in size (20x20) is made convolution to the input image, the output image has softened too much and the blur is quite high. When looked at matrix values, matrix values in the same regions are close to each other. Considering these results, we can say that when the size of the kernel applied to the input image is increased, the image becomes more soft and blurred.

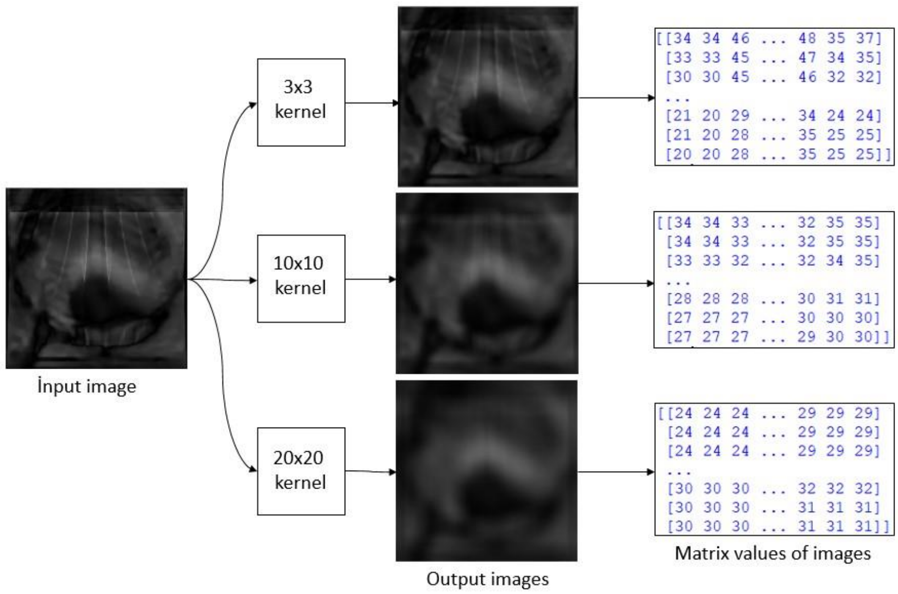

Figure 3.8. The result images and matrix values when the mean filter is applied to the input image.

3.2.2.2. Median Filter

Median filter reduces the noise as in the mean filter, however, the details are more hidden in the median filter. When finding pixel values in the median filter, the neighboring pixel values are sorted from small to large and the pixel value in the middle of the line is replaced with the current pixel value. If there are two values in the middle of the row, the pixel value is the average of these two values. Unlike the mean filter, the median filter is a nonlinear filter. The median filter filters each pixel in the image and it is used to decide whether its neighbors represent its surroundings (Boateng, Asubam, & Laar, 2012). The kernel value must be a positive odd number in the median filter. In the following image, the example of the calculation of the median filter is shown.

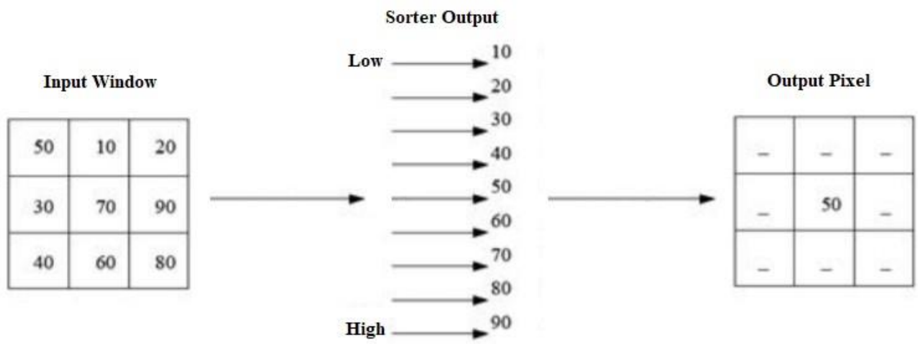

Figure 3.9. Change of the center pixel value in the area covered by the core matrix when a median filter is applied to the input image (Boateng et al., 2012).

Examining the figure 3.9, a beginning pixel is selected and the pixels around this pixel are analyzed. A 3x3 pixel window, kernel, is used to calculate the output, and pixels belonging to the input image are sorted and the median pixel value is found as 50. This value is replaced by the value that is 70 in the input image, and it became 50 at the output.

On the second day, when the median filter is applied to the fifth layer image with different kernel values, the result images are shown in Figure 3.10. When Figure 3.10 is examined, it is seen that when the median filter with kernel values of 5, 9, and 15 are applied to the input images, the noise is reduced and the corners are preserved at the output. Also, according to the kernel size applied, it is understood that the blur increases at the output. When the size of the applied kernel value increases, it is seen that the matrix values of the output image converge.

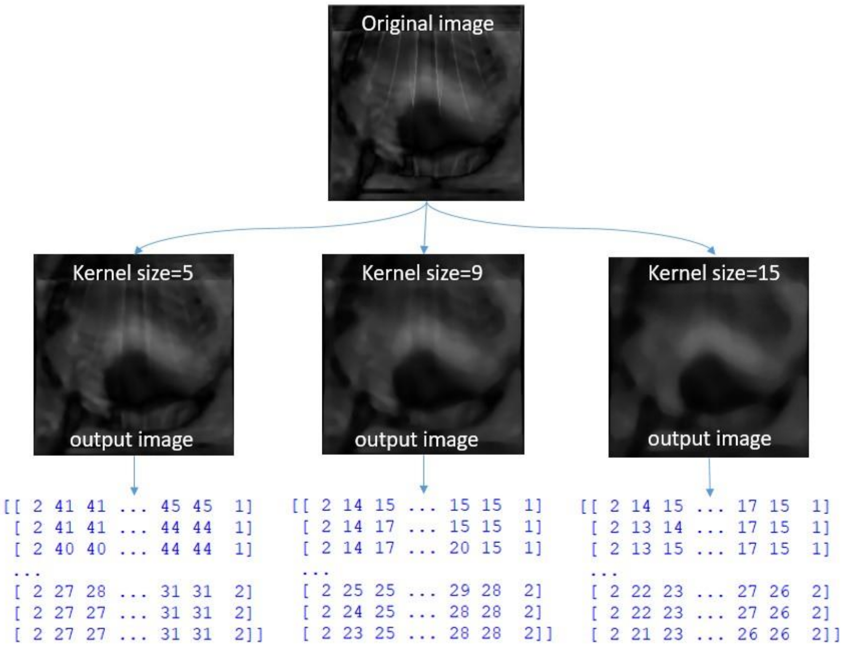

Figure 3.10. Result images and matrix values when a median filter is applied to the input image.

3.2.2.3. Bilateral Filter

Bilateral filtering, which is quite efficient in noise removal protects the edges as in the median filter. Bilateral filtering which is non-iterative, local, and simple method combines gray values and colors based on both their geometric proximity and photometric similarity and prefers values that are closer than distant values in both area and range (Tomasi & Manduchi, 1998). The logic of the bilateral filter is that in order for a pixel to affect another pixel, the pixel should not only occupy a nearby location but also have a similar value (Paris, Kornprobst, Tumblin, & Durand, 2009). The bilateral filter is formulated as follows.

$$BF[I]_p = \frac{1}{W_p} \sum_{q \in S} G_{\sigma_s}(||p-q||)\, G_{\sigma_r}(||I_p - I_q||) \tag{4}$$

The value of W_p is the normalization factor and this value ensures that the sum of the pixel weights is 1. The parameters σ_s and σ_r determine the amount of filtering for the image. G_{σ_s} is the normalized weighted average value that reduces the effect of distant pixels. G_{σ_r} value is a

Gaussian ratio that reduces the effect of q when the density value differs from I_p (Paris et al., 2009).

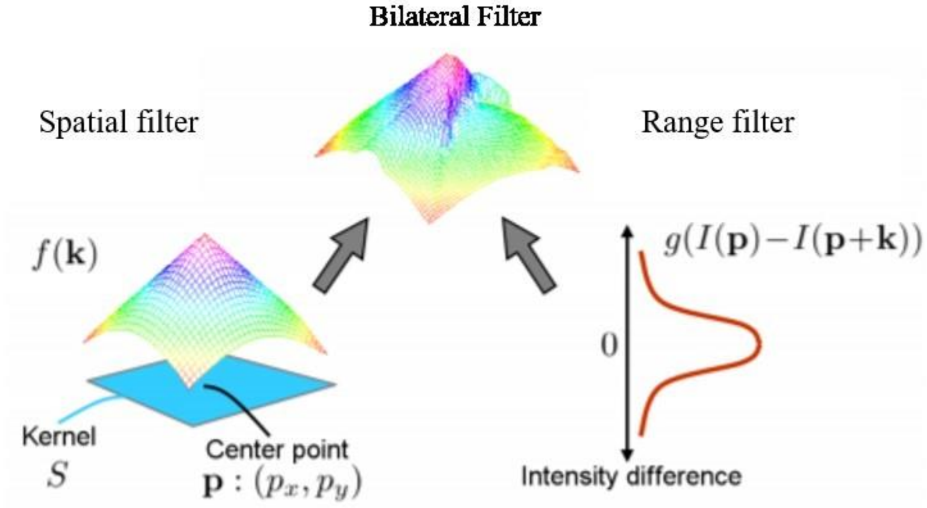

Figure 3.11. Structure of bilateral filter with spatial filter and range filter (Porikli, 2008).

When looking at Figure 3.11, it is seen that the bilateral filter consists of a combination of spatial filter and range filter. When the figure is examined, the bilateral filter multiplies a range filter with the density value of an image point in the S kernel corresponding to the spatial filter coefficient f (k) (Porikli, 2008).

3.2.2.4. Gaussian Filter

Gaussian filtering has been extensively studied in filtering, image processing, and computer vision. Using the Gaussian filtering for noise suppression, noise is softened and it is an important filtering method for edge detection (Deng & Cahill, 1993). The Gaussian filter which is used to blur images, remove noise and details is a non-uniform low pass filter that softens the image by calculating the weighted averages in a filter box. The equation 5 gives one dimensional Gaussian function and equation 6 gives two dimensional Gaussian function. In the equation, sigma (σ) represents standard deviation and the distribution is assumed to be an average equal to zero (Julio, Soares, Costa, & Bampi, 2015).

$$G(x, y) = \frac{1}{2\pi\sigma^2} e^{-\frac{x^2}{2\sigma^2}} \quad (5)$$

$$G(x,y)=\frac{1}{2\pi\sigma^2}e^{-\frac{x^2+y^2}{2\sigma^2}} \tag{6}$$

In one-dimensional and two-dimensional Gaussian functions, Gaussian core coefficients depend on the value of σ (Julio et al., 2015).

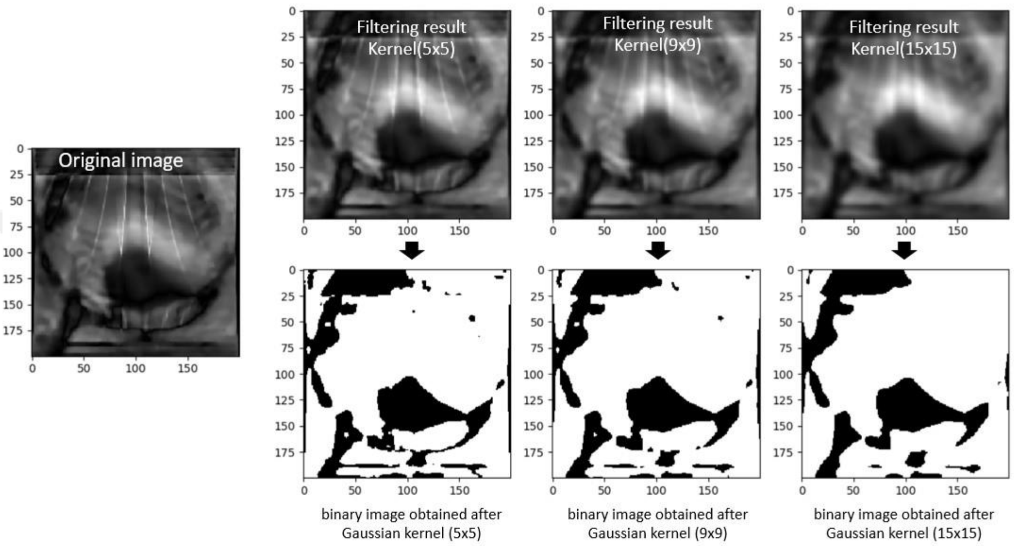

Figure 3.12. When the different size of the Gaussian filter is applied to the original image, the result images and the binary images obtained from the result images.

When the Gaussian filter which is different kernel size is applied to the second layer of the spheroid structure on the second day, the result images are shown in Figure 3.12. It is observed that when the filter with a larger core size is applied to the input image, the softening in the image increases and unnecessary details disappear in the binary image.

After applying the above-mentioned filters separately to the layers of the spheroid structure converted to gray format, it was seen that the most efficient filter we should use in our study was the Gaussian filter. After applying the filter, contrast noise ratios of the images were measured. CNR (Contrast to noise ratio) per pixel was calculated as a measure of the detectability of the main tumor structure in the image. CNR ratio is defined in equation 7 (Polat et al., 2018).

$$CNR = \mu_{ROI} - \mu_{Background} \tag{7}$$

$$\sigma_{Background}$$

When equation 7 is examined, μ_{ROI} and $\mu_{Background}$ values are the average values of the main tumor structure and background within the image, respectively. The value of $\sigma_{Background}$ is the standard deviation of the image background. When the CNR formula was calculated separately for each filter using the fifth layers of Day 2, Day 4, and Day 6, it was observed that the Gaussian filter best separated the main tumor structure from the background. Numerical values obtained using CNR are shown in table 3.1.

Table 3.1. CNR values obtained as a result of filters applied to the second, fourth and sixth day images.

Area	Mean	Std. Dev.	Min	Max
18.909	46.279	23.428	0	145
18.909	46.240	23.895	0	119
18.909	45.748	24.555	1	111
18.909	46.231	22.768	0	118
18.909	45.229	22.740	1	118
Area	Mean	Std. Dev.	Min	Max
16088	49.941	18.417	0	121
16088	49.937	18.027	1	104
16088	49.517	18.714	1	100
16088	49.935	17.939	1	102
16088	49.932	18.915	1	102
Area	Mean	Std. Dev.	Min	Max

ROI BACKGROUND CNR

	Area	Mean	Std. Dev.	Min	Max						VALUE
2nd day Raw image	3.120	13.696	10.056	0	76						**1,39**
2nd day Mean filter	3.120	13.810	9.929	0	58						**1,36**
2nd day Median filter	3.120	13.746	9.766	1	57						**1,30**
2nd day Gaussion filter	3.120	13.866	9.891	0	57						**1,42**
2nd day Bilateral filter	3.120	13.874	9.880	0	57						**1,38**
	Area	Mean	Std. Dev.	Min	Max						
4th day Raw image	17.947	13.883	0	81	81						**1,96**
4th day Mean filter	4680	17.989	13.734	0	79						**1,77**
4th day Median filter	4680	17.846	13.578	1	74						**1,69**
4th day Gaussion filter	4680	18.006	13.699	1	77						**1,78**
4th day Bilateral filter	4680	18.012	13.690	1	77						**1,69**
	Area	Mean	Std. Dev.	Min	Max						
6th day Raw image	2844	11.496	7.980	0	39	14824	43.920	18.296	0	114	**1,77**
6th day Mean filter	2844	11.527	7.837	0	38	14824	43.916	19.033	0	112	**1,70**
6th day Median filter	2844	11.566	7.786	0	39	14824	43.704	17.954	0	112	**1,79**
6th day Gaussion filter	2844	11.553	7.794	0	38	14824	43.915	17.945	0	112	**1,80**
6th day Bilateral filter	2844	11.558	7.785	0	38	14824	43.914	18.925	0	112	**1,71**

CNR values obtained as a result of filters applied to the second, fourth and sixth day images.

3.3. Segmentation

In the detection of cancer cells, after the image pre-processing step is applied, the segmentation phase is started. In the segmentation part, the objects in the image are completely separated from the background and so, it becomes easier to detect and diagnose cancerous cells. The processes used in the segmentation step are thresholding, morphological operations, and contour area drawing steps. Segmentation steps on cancerous cell images we use in the study are described below.

3.3.1. Thresholding Process

The thresholding process which converts grayscale images to binary images, distinguishing objects from the background is the most effective and easy way to separate an image into a foreground and background (Borole et al., 2015). The image must be converted to a gray format before applying the thresholding on the images. In the global thresholding process, the object value in the image is compared with a threshold value (T) and the object is then separated from the background by a simple operation. The histogram of an image with a value of f (x, y) is shown in figure 3.13.

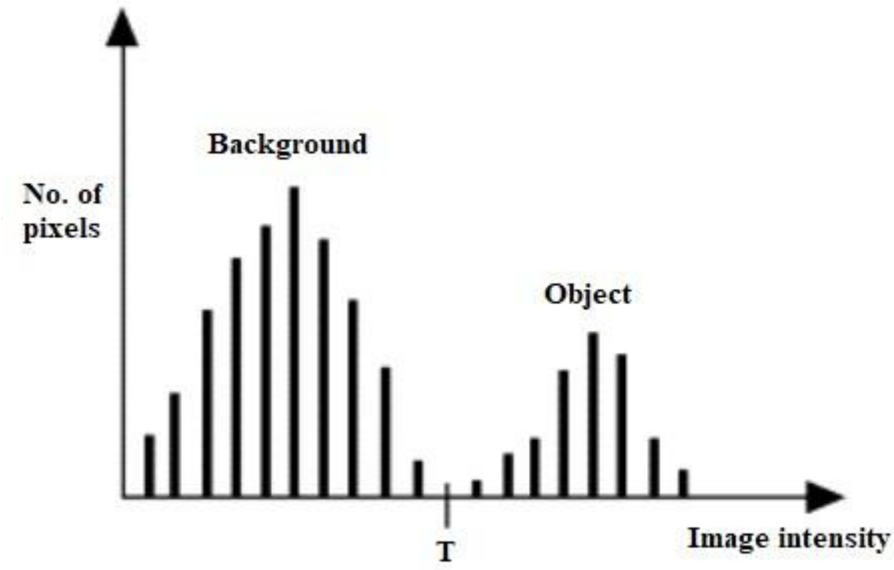

Figure 3.13. Image graphic divided into two parts according to the selected x value (Rogowska & analysis, 2000).

When Figure 3.13 is examined, the gray levels of the object and background pixels are grouped in two modes. The way to separate the object from the background is to choose a T threshold value that separates these modes (Rogowska & analysis, 2000). If we say g(x, y) for the image obtained after the threshold and s(x, y) for the source image, the thresholding process is formulated as follows. This thresholding method is the simplest thresholding method.

$$g(x,y) = \{ \quad 1, \qquad s(x,y) > T \qquad (8)$$

$$0, \qquad s(x, y) \leq T$$

After the thresholding process, a binary image is obtained. In this image, pixels that density value is 1 represent the object and pixels that density value is 0 represent the background. If a pixel value in the image is greater than the threshold value, this pixel value becomes 1, otherwise, the pixel value becomes 0. Figure 3.14 shows the threshold view of rice grains. In this image, white rice grains are objects, and the black parts are background. With small changes, it is possible to make rice grains black and it is possible to make background white.

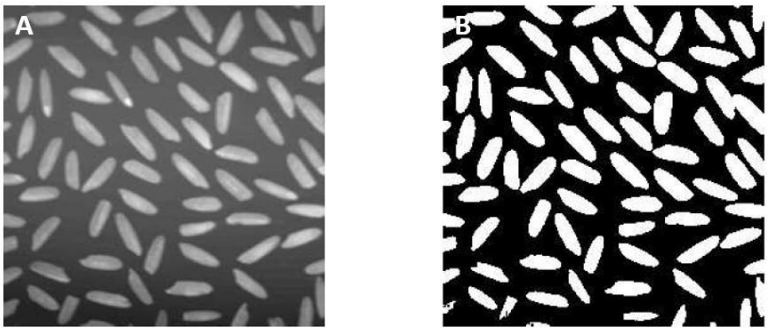

Figure 3.14. Threshold view of rice grains. After the thresholding process, the rice grains became the object and the black sections became the background (McAndrew & Mathematics, 2004).

Another thresholding method is adaptive thresholding. If an image has different lighting conditions in different areas, it may not be possible to set a single threshold to separate the object from the background. In this case, different threshold values are determined for different regions of the image. In the adaptive thresholding process, the image is divided into small pieces and a threshold operation is applied to each piece separately (McAndrew & Mathematics, 2004). Figure 3.13a, when simple thresholding is applied to the image, the right side of the image disappears completely. Therefore, applying simple thresholding on this image will give an unsuccessful result. In this case, as seen in Figure 3.15c, the image is divided into small pieces and separate threshold values are applied for each piece. As a result, the binary image is obtained as in Figure 3.13d.

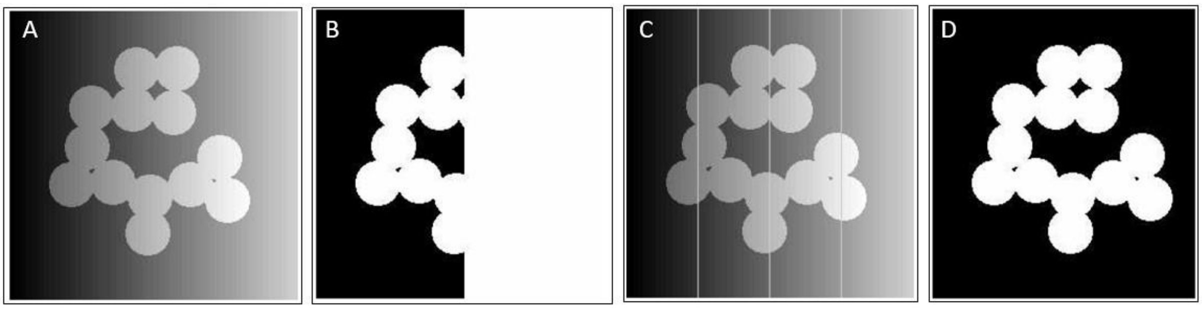

Figure 3.15. Application of adaptive thresholding method. (A) Original image. (B) Simple thresholding result. (C) Image fragmentation. (D) Adaptive thresholding result (McAndrew & Mathematics, 2004).

We set the threshold value ourselves in the simple thresholding process, also known as Global thresholding. As sometimes the value we choose may not give the desired result, we try to find the appropriate value by trial and error method. Otsu's method calculates the appropriate threshold for bimodal (the image with two vertices in the histogram), that is, Otsu's binarization method automatically calculates the threshold value based on the image histogram for a bimodal image (Mordvintsev & Abid, 2017).

In Figure 3.16, the global thresholding method is applied to a noisy image but the resulting image is unsuccessful. At the same time, the result obtained by applying the Otsu method on the noisy image is also unsuccessful. Because, in the image histograms, there is a peak value for both images. Looking at the image histogram of the image with a Gaussian filter, it is seen that there are two peaks. In this case, Otsu's method will give a successful result and a smooth binary image has been obtained when looking at the resulting image. Looking at the equation below, the α ve μ_1 values are the ratio of the pixels that are darker than the threshold value and the average brightness value, respectively. The β ve μ_2 values are the ratio of the pixels and the average brightness value that brighter than the threshold value. The herbaceous method automatically calculates the 'T' threshold value described in the equation below to maximize inter-class variance (Jeong, Park, & Park, 2017).

$$\sigma_T = \alpha\beta(\mu_1 - \mu_2)^2 \tag{9}$$

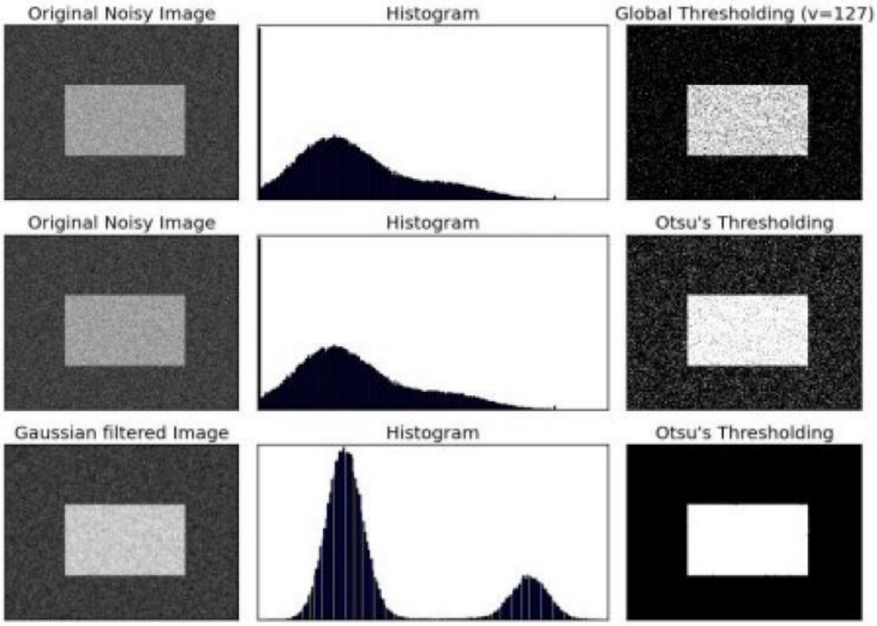

Figure 3.16. Application of the Otsu's thresholding method on original noisy and gaussian noisy images (Mordvintsev & Abid, 2017).

In the thesis study, after the images with spheroid structures were converted to grayscale images, and noise reduction was applied, various image thresholding methods were applied to the images. On the fourth day, the result of the thresholding methods applied in the tenth layer image is shown in Figure 3.17. When the results of the thresholding methods are examined, it is concluded that the most suitable thresholding method for spheroid images is global thresholding. In the adaptive thresholding method, as a result of the thresholding applied to different parts of the image, the main mass was not separated from the background and a highly unsuccessful result was obtained. In Otsu's binarization method, an average threshold value was calculated for the gray image, but this value also perceived the sections outside the main mass as objects. Therefore, Otsu's binarization method is not a suitable method for the images with spheroid structures we use in our study.

Figure 3.17. Results of the thresholding methods applied to the spheroid image. (A) Original image. (B) Global thresholding result. (C) Adaptive thresholding result. (D) Otsu's binarization result.

3.3.2. Morphological Operations

Mathematical morphology is a powerful image processing analysis in nonlinear neighborhood operations. When applying morphological processing on an image, there are two basic operations used: dilation and erosion. Other processes are opening and closing processes obtained using these two operations (Boztoprak, Çağlar, & Merdan, 2007).

3.3.2.1. Dilation

In the dilation process, the objects in the image expand according to the structural element. Moving the structural element over the input image, that is, performing convolution, is called dilation. The structural element determines how much the expansion will be on the input image (Raid, Khedr, El-Dosuky, Aoud, & Technology, 2014). Assuming that A is the input image and B is the structural element, A's dilation by B is expressed by the following formula (Gonzales & Woods, 2002)

$$A \oplus B = \{z \mid (\hat{B})_z \cap A \neq \emptyset \} \qquad (10)$$

Looking at the above statement, object A expands according to the size of the structural element B when the center of the structural element and the pixel value of the object overlap. If there is no intersection, there is no enlargement on the object in image A. In Figure 3.18, the image was enlarged.

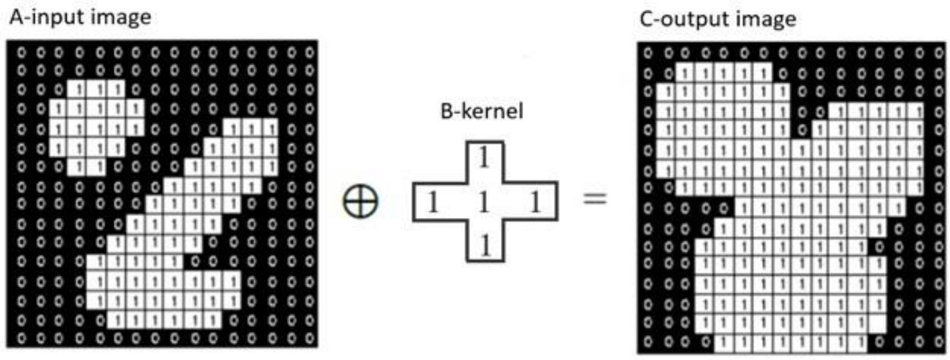

Figure 3.18. Expansion of the input image as a result of using structural elements (Raid et al., 2014).

3.3.2.2. Erosion

In erosion, which is one of the basic operations of mathematical morphology, the boundaries of the target object are eroded. The erosion process is partly the reverse of the dilation process. The objects in the target image become smaller, if there are holes, they expand, and the connected objects begin to separate (Karhan, Oktay, Karhan, & Demir, 2011). If we consider A as the input picture and B as the structural element, the erosion of A by B is shown as follows.

$$A \ominus B = \{z \mid (\hat{B}) \subseteq A \qquad (11)\ z$$

The erosion of A by B is as in equation 11. First, the structural element B is navigated in A. If all the values of B overlap with the object in A, the pixel value of the object corresponding to the center pixel of B is deleted. Otherwise, the pixel value of object A remains the same. Figure 3.17 where a 3x3 matrix value kernel is used shows the image formed by the eroding of image A with the structural element B.

3.3.2.3. Opening and Closing

The opening is performed as a result of applying erosion and dilation processes respectively on the image. Thus, the holes between the objects in the image are cleaned according to the size of the structural element by the opening operation (Karhan et al., 2011). The application of the erosion process immediately after the dilation process on the image is called the closing. With this process, objects that are close to each other in an image are connected to each other (Özşen, 2002). The opening process is expressed by the "□" sign. The sign " □ " is used for closing.

Opening and Closing operations are shown in equations 12 and 13, respectively.

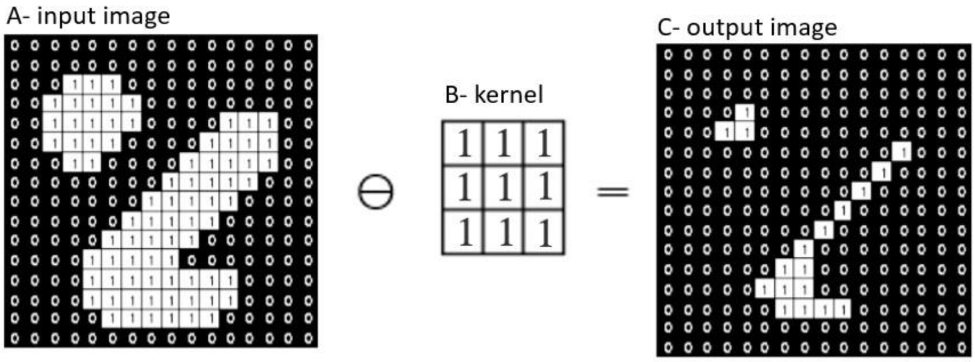

Figure 3.19. Eroding of the input image as a result of using 3x3 structural element (Acar & Bayram).

$$A \circ B = (A \ominus B) \oplus B \tag{12}$$

$$A \bullet B = (A \oplus B) \ominus B \tag{13}$$

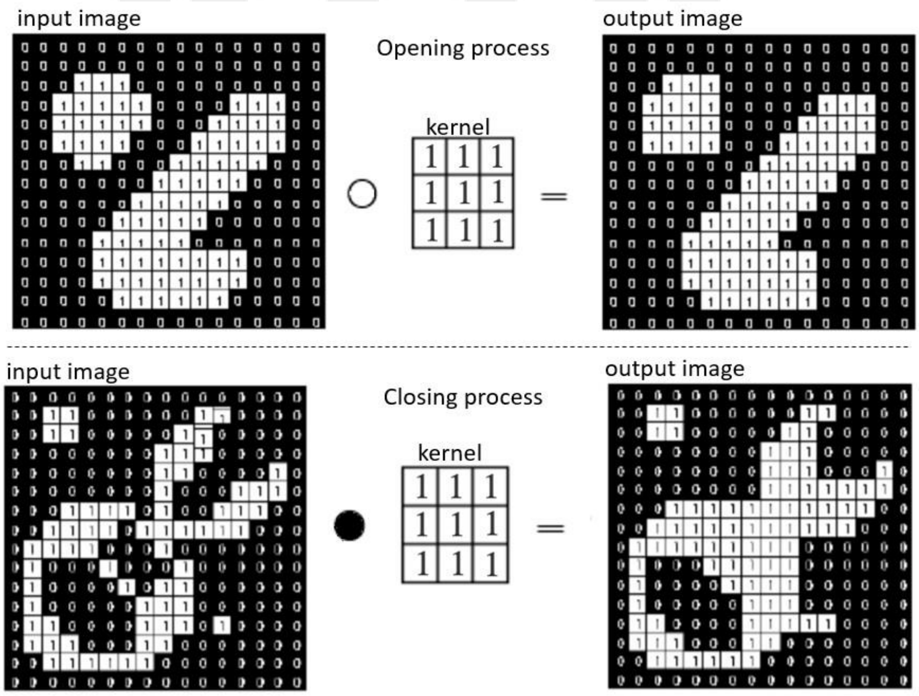

Figure 3.20. Representation of opening and closing processes (Raid et al., 2014)

In the thesis study, in order to reach the main tumor masses in the images taken on the second, fourth, and sixth days, the images went through morphological stages after thresholding. For each of the 30 images, one or more of the dilation, erosion, opening and closing operations were used. Thus, the limits of the main mass were tried to be reached as much as possible.

In Figure 3.21, after the thresholding operation was applied, erosion was applied to the fifth layer image on the second day. After applying erosion, the main tumor mass shrank unwanted. To get rid of this undesirable condition, dilation was applied after erosion and the desired tumor structure was reached. In Figure 3.22, after the original image was converted into a binary image, firstly, dilation operation was applied to the image but a view far from the main tumor structure in the input image occurred. Then, the closing operation was applied to the binary image and the main tumor mass at the size close to the input image was obtained. As a result, morphological operations were used when needed in our study.

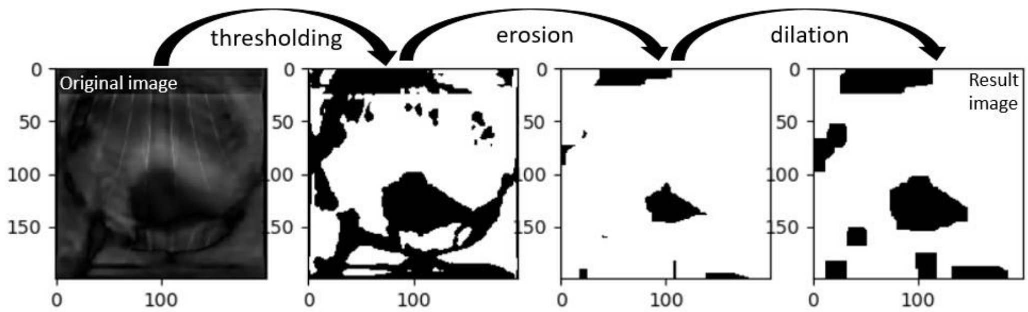

Figure 3.21. Applying morphological operations which are called erosion and dilation to the original image, respectively, and obtaining the output image.

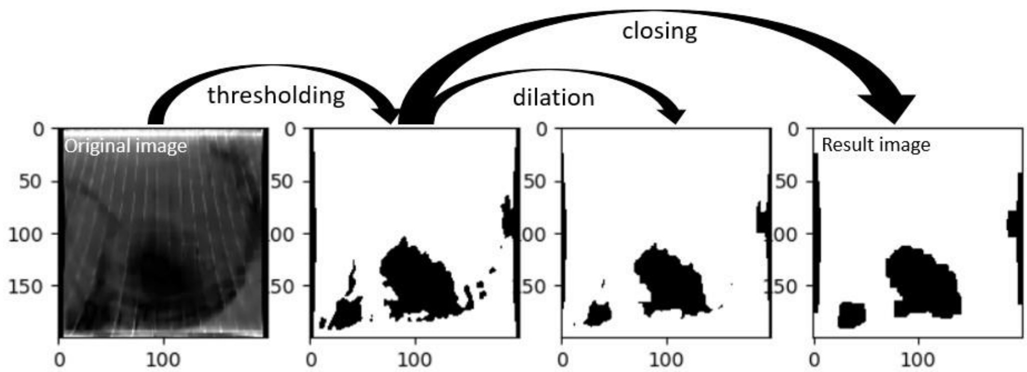

Figure 3.22. Applying morphological operations which are called dilation and closing to the original image, separately and obtaining the output image.

3.3.3. Contour Tracking

Contour tracking, also known as border tracking, is the process of drawing the boundaries of a region of pixels that have the same color or density and so, a series of boundary points are obtained (Rao, Lin, Xu, & Lin, 2012). To draw contour boundaries, it is necessary to be known the coordinates (x, y) of object boundaries. After the contour coordinates of the object's boundaries are found, the contour boundary is drawn for the object. But there is no need to keep all the coordinates of the object because this situation occupies memory unnecessarily. To get rid of this situation, only the two endpoints of the flat boundaries of the object are stored (Mordvintsev & Abid, 2017). In this case, the limit coordinates required by the change in the contour approach parameter in the cv2.findContours () function is stored in the OpenCV environment. In Figure 3.23, all coordinates of the border are reached in the image on the left, and this image has more than 100 contour points. In the image on the right, only the required contours are in the corners and the total number of coordinates is four points, which are shown in blue colors. Therefore, the image on the right occupies less memory.

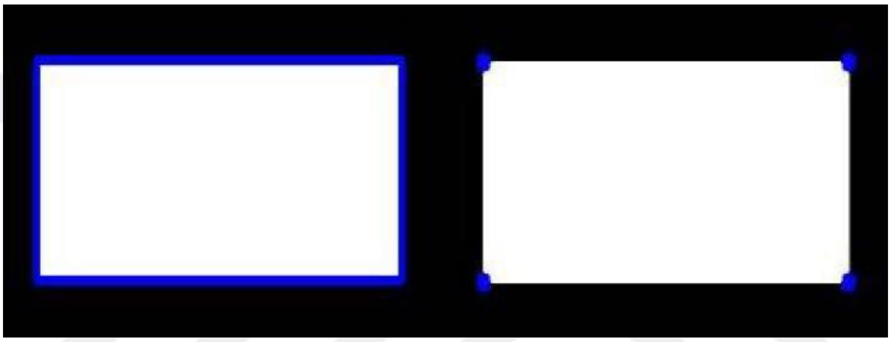

Figure 3.23. Effect of contour approach method on images (Mordvintsev & Abid, 2017).

Contour tracking, which is frequently used in areas such as image processing, image repair, and image recognition, has many contour tracking algorithms, some of which provide highly accurate results (Xie et al., 2013). In our thesis, we used the functions of the OpenCV library for contour monitoring.

In our study, after the pre-processing step was applied for the layers we used, thresholding and morphological operations were applied in the segmentation stage. After the main tumor mass has been obtained, boundary lines called contours were automatically drawn for each image to highlight these masses. Figure 3.24 shows the cancerous image belonging to the 40th layer on the second day. In Figure 3.24d, approximately 14 border lines were drawn on the cancerous image. The regions whose borders are drawn are regions with a color similar to the color density of the cancerous image. Since the aim is to reach the main tumor mass, areas except the main tumor mass were eliminated and the borderline of the main tumor mass is automatically drawn, as in 3.24e.

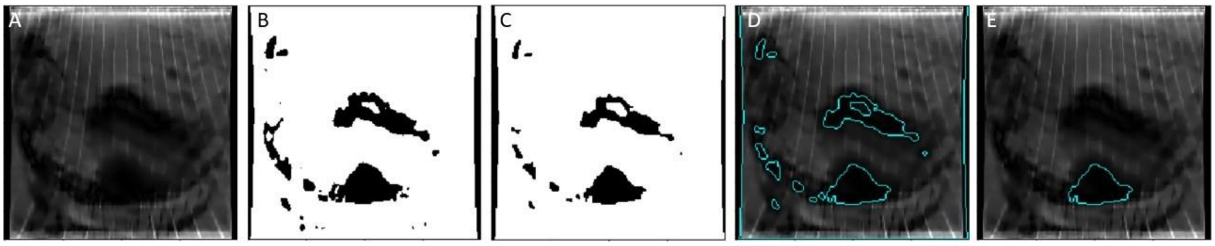

Figure 3.24. Drawing the contour boundary for the main tumor mass. A) Original image. B) Binary image obtained after thresholding. C) Applying erosion to the binary image. D) More than one contour drawing. E) Automatic plotting of the boundary line for the main tumor mass.

3.3.4. Edge Detection

Edge detection is used to find boundaries in an image and is a very useful algorithm. In fact, edge detection is similar to contour tracking. Sobel, Canny, Prewitt, Log, and Zero cross methods are widely used to find the boundaries of an object (Borole et al., 2015). The Canny Edge Detection algorithm developed by John F. Canny was used in our study. Since edge detection is sensitive to noise in the image, unnecessary objects and noise in the image must be cleaned before using this operator. For this, the image is filtered and it is taken derivative in horizontal and vertical directions of the filtered image. Thus, it is possible to find the edge gradient and direction for each pixel with the following two formulas (Li, Jevtic, Söderström, Ur Réhman, & Li, 2013). Here, G_x and G_y are the derivative values in the horizontal and vertical directions. G is the gradient size. The value of θ determines the direction of the pixel value with the gradient.

$$G = \sqrt{G_{x}2 + G_{y}2} \tag{14}$$

$$\theta = \arctan\left(\frac{G_x}{G_y}\right) \tag{15}$$

Figure 3.25 shows the output images obtained by applying Edge Detection in the original, noisy, and noiseless situations of the 40th layer of the second day. As seen in 3.25d, the number of limits has been reduced by algorithm applied after removing the noise. This event reduces the amount of data in the image, and the number of operations.

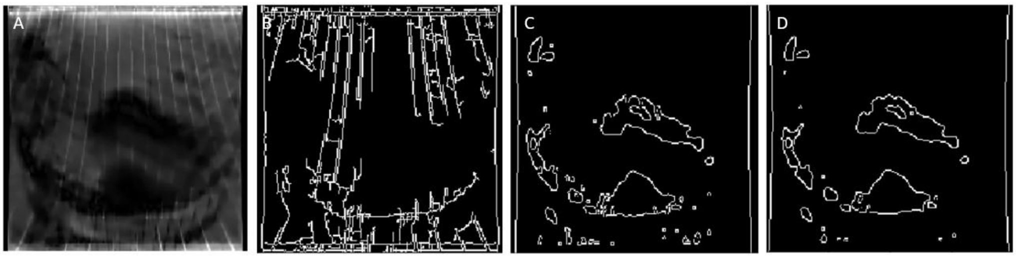

Figure 3.25. A) Original image. B) Applying edge detection to the original image. C) Applying edge detection to noisy+binary image. D) Applying edge detection to noiseless + binary image.

3.4. Feature Extraction

After the preprocessing and segmentation stages, the main tumor masses in cancerous images were detected. The step handled in this section is the "Feature Extraction" step, which has an important place in image processing. Feature extraction is the section where the features of the images such as color, texture, shape are discussed (Mohanaiah et al., 2013). Based on these features, it is possible to make various assumptions about the image or objects within the image. By using the data obtained by applying Feature Extraction on the images, these data can be trained in the next stages and thus classification can be made (Abdoulaye & Demir, 2017). In the thesis study, geometric feature extraction procedures were performed by calculating values such as area, perimeter, radius for the main tumor structures in the layers belonging to the second, fourth, and sixth days of three-dimensional cancerous images obtained from the miniOpto tomography device. These feature extractions are listed below.

3.4.1. Contour Area Calculation

In the feature extraction step, firstly, the area of the main tumor masses which are the sum of the pixels within the contour limits in pixels was first calculated. For the second, fourth, and sixth-day images, after the contour boundaries of the main tumor masses were automatically drawn, in order to examine how much these masses grew on different days, the area in pixels of each image was calculated. To calculate the area, it is necessary to find the moment which is used to calculate some values such as area and center of mass of the relevant object in the image (Mordvintsev & Abid, 2017). The value of zero moment, m_{00}, gives the sum of the pixels in an object, that is, the field value. The first-order moments, m_{10}, and m_{01} are used to determine the position of an object. Another way to calculate the total are value in an image is to use the contourArea () function in the OpenCV library. With this function, it is possible to calculate the area in pixels. If I (x, y) is a digital image, the μ value is the central moment of the digital image. Here, $\bar{x}$ and $\bar{y}$ are the components of the centroid (Zhang et al., 2015).

$$\mu_{mn} = \sum_x \sum_y (x - \bar{x})^m (y - \bar{y})^n I(x, y) \tag{16}$$

$$\bar{x} = M_{10} / M_{00}\ , \qquad \bar{y} = M_{01} / M_{00} \tag{17}$$

3.4.2. Contour Length Calculation

The contour length of the main tumor masses is one of the parameters used to understand the characteristics of these masses. Each layer of three-dimensional images obtained on different days is of different length. The sum of the pixels within the closed contour border surrounding the tumor structures gives the perimeter.

3.4.3. Diameter Drawing

Another parameter used to extract geometric features is the radius measurement for diameters that surround the main tumor masses in an optimal way. This feature gives radius growth values of tumors from the second day to the fourth day and from the fourth day to the sixth day. Radius measurement is an important parameter in evaluating the growth development of tumors.

Figure 3.26 shows the images belonging to the 40th layer on the fourth day. While the perimeter value is the sum of the pixels surrounding the main mass, which is approximately 277.095 pixels, the area value of the main mass is the sum of the pixels within the contour limits and its value is 3746.5 pixels. The circumference value is not directly related to the radius because the main mass is an irregular shape. But for some spheroid structures, the result of 2πxRadius is very close to the Perimeter value. This indicates that although the main mass grows irregularly, it grows at a value close to the circle surrounding the main mass as a minimum.

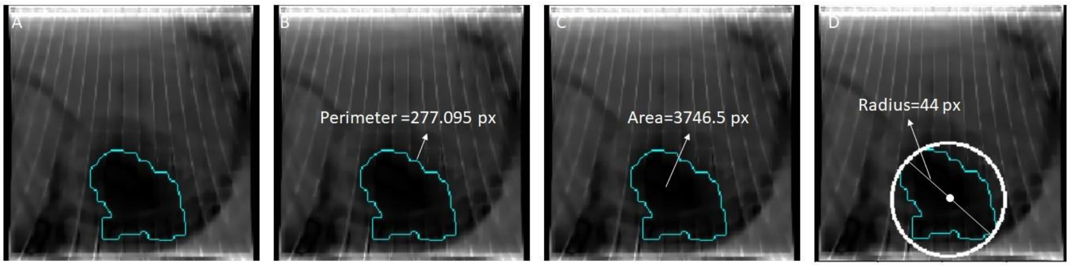

Figure 3.26. The geometrical feature extraction of cancerous images. A) Original image. B) Contour perimeter in pixel. Perimeter is the sum of the pixels of the contour boundaries. C) Contour area. The contour area is the sum of the pixels within the boundaries surrounding the main tumor mass. D) Circle radius. The circle radius is the radius of the circle that minimally surrounds the main tumor mass.

4. RESULTS AND DISCUSSIONS

The images were divided into two-dimensional layers by using the ImageJ program to examine the growth development of the main tumor structure of the three-dimensional cancerous images obtained on the second day, the fourth day, and the sixth day. Area, perimeter, and diameter measurements were made for these structures in pixels after the main mass in each layer was automatically separated by the boundary lines called contours. Manually drawn images of the contour borders are shown in section 3. The contour boundaries drawn automatically in the Pyhton-OpenCV environment are shown in Figure 4.1.

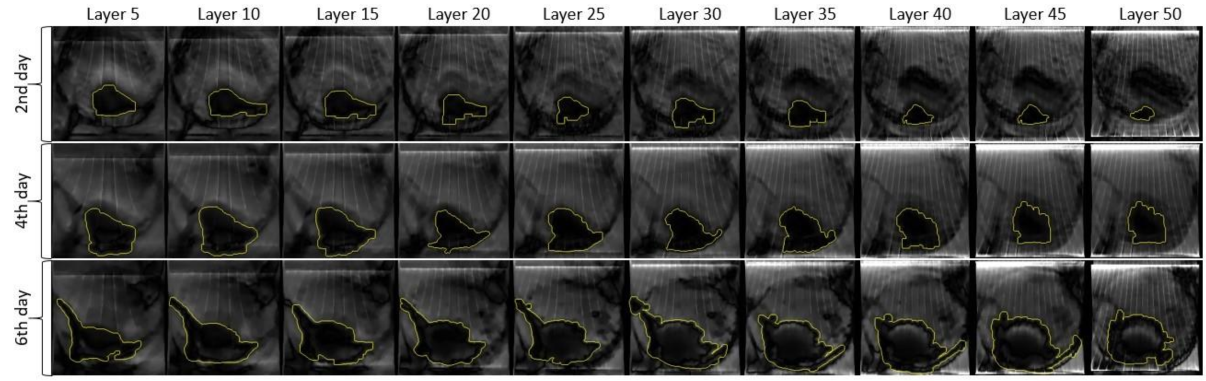

Figure 4.1. For the images belonging to the second, fourth, and sixth days, the main tumor masses that the contour boundaries are automatically drawn.

After the borders were automatically drawn, the following measurements were made to observe the volumetric changes of the main tumor masses and to comment on their characteristic features.

4.1. Area Measurements

Area measurements for 30 layers on the second, fourth, and sixth days are given in Table 4.1. It is possible to find the approximate volumes of three-dimensional main tumor structures by summing the cross-sectional area values of 10 two-dimensional layers obtained for each day. Therefore, the volume value of the three-dimensional main tumor mass for the second day is 20055 pixels, the volume value of the main tumor structure on the fourth day is 44466 pixels and the volume value of the main tumor structure for the sixth day is 82622 pixels. The volumetric growth of tumor structures from the second day to the fourth day, from the fourth day to the sixth day and from the second day to the sixth day can be calculated as a percentage by using the volumetric values belonging to each day. According to the results obtained from the total volumes, the volumetric growth rate from the second day to the fourth day is 121 percent. Volumetric growth from the fourth day to the sixth day is 85 percent and volumetric growth from the second day to the sixth day is 311 percent. Considering the approximate volumetric growths based on the field sections, it is seen that main tumor structures show irregular growth rates.

Table 4.1. Area values of main tumor structures of the second, fourth, and sixth days in pixels.

	2nd day areas in pixel	4th day areas in pixel	6th day areas in pixel
Layer 5	2833,5	5049	6082
Layer 10	3072,5	5906,5	7512,5
Layer 15	2978	5638	7500
Layer 20	2379	3835,5	7745,5
Layer 25	1657,5	4808	7777
Layer 30	2370	4076	9663,5
Layer 35	2052	4733,5	8977
Layer 40	1105	3746,5	9364,5
Layer 45	973	3515	10019
Layer 50	634,5	3158	7981

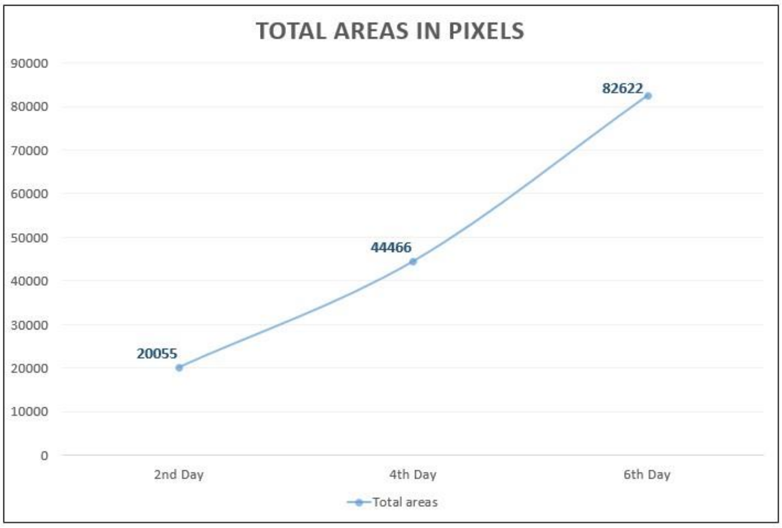

Figure 4.2. Total area values in pixels for the second, fourth and sixth days.

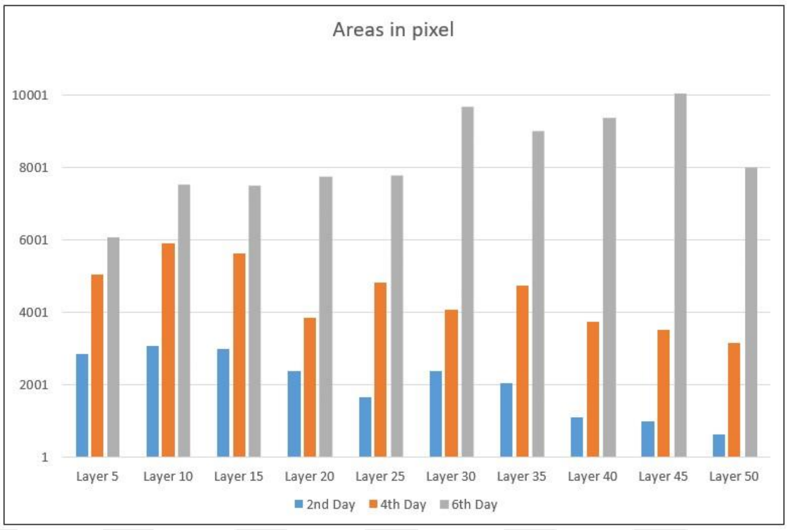

Figure 4.3. Area values of main tumor masses belonging to the layers of spheroid structures on the second, fourth, and sixth days.

4.2. Perimeter Measurements

Just starting from volumetric growth, commenting on the type of cancerous structures can give misleading results. In the thesis study, the perimeter values, which are the sum of the perimeter pixels of main tumor structures in three-dimensional images obtained for three days, were calculated. Contour perimeter values are shown in table 4.2.

Table 4.2. Perimeter values in pixels of main tumor structures on the second, fourth, and sixth days.

	2nd day perimeters in pixel	4th day perimeters in pixel	6th day perimeters in pixel
Layer 5	222.953	303.137	505.303
Layer 10	271.438	330.693	473.060
Layer 15	255.539	334.450	451.220
Layer 20	242.083	334.634	481.203

Layer 25	187.639	312.793	510.274
Layer 30	240.710	327.563	612.658
Layer 35	210.568	352.291	521.587
Layer 40	157.882	277.095	556.173
Layer 45	141.740	271.882	578.274
Layer 50	113.840	260.367	457.421

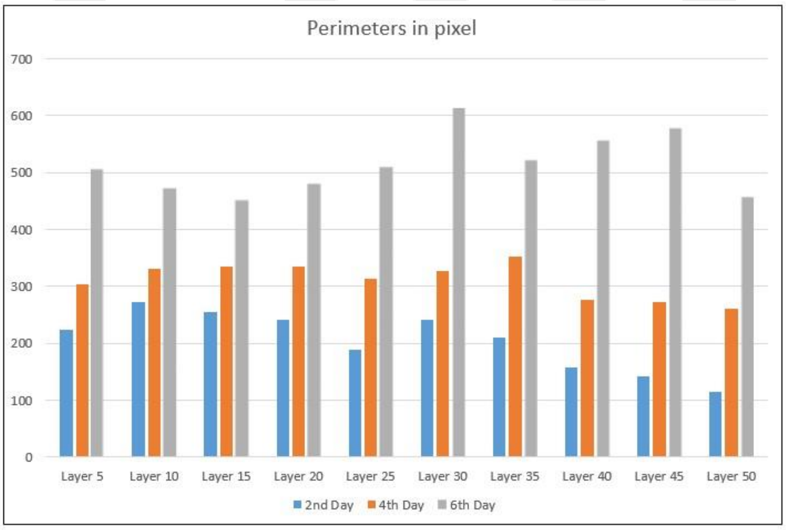

Figure 4.4. Perimeter growth values of main tumor masses belonging to the layers of spheroid structures on the second, fourth, and sixth days.

Looking at Table 4.2, the perimeter values of main tumor structures grew from the second day to the fourth day and from the fourth day to the sixth day. The graphical representation of the perimeter growth of the main tumor structures is given in figure 4.4. When the graphic is carefully examined, perimeter values from the second day to the sixth day increased nonlinearly for all layers. Volumetric values belonging to three-dimensional structures cannot be calculated using perimeter values but in future studies, the values such as the perimeter, radius, etc will be more important in classification studies.

4.3. Radius Measurements

After the area and perimeter calculations were made for the layers of cancerous structures, circles surrounding the main tumor structures in a minimum manner were drawn. Since cancerous structures have irregular shapes, it is impossible to calculate the diameter of these structures. For this reason, circles surrounding the cancerous structures as minimum were drawn, and approximate diameter growths of main tumor structures were calculated after the circles were drawn automatically. Radius values are shown in table 4.3 and the graphical representation of radius enlargements is given in figure 4.5. Looking at Figure 4.5, the radius values for all layers increased continuously from the second day to the fourth day and from the fourth day to the sixth day. This situation shows that the tumor structures used in the study tend to grow continuously.

Table 4.3. Radius values in pixels of main masses on the second, fourth, and sixth days.

	2nd day radius in pixel	4th day radius in pixel	6th day radius in pixel
Layer 5	39	51	83
Layer 10	52	55	86
Layer 15	46	56	78
Layer 20	40	55	83
Layer 25	30	52	84
Layer 30	37	52	96
Layer 35	33	52	80
Layer 40	27	44	82
Layer 45	26	42	80

Layer 50	20	40	63

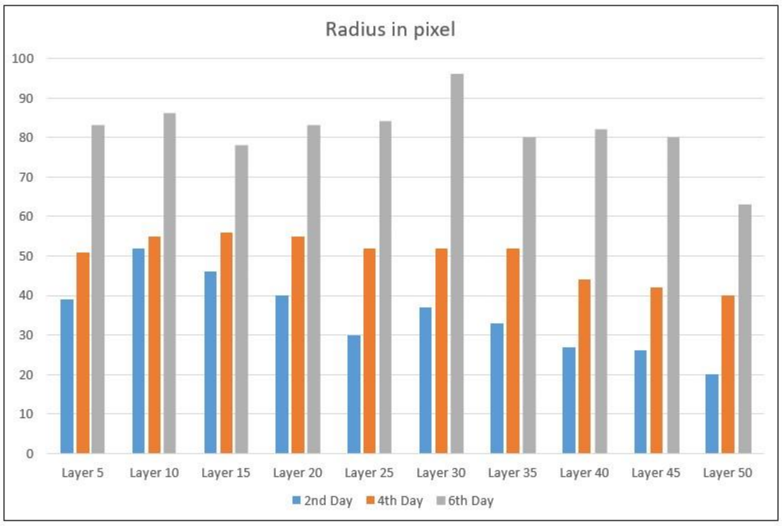

Figure 4.5. Radius values for the circles surrounding as minimum the main tumor structures that belong to the second, fourth, and sixth days.

When looking at the measurement results for three different days, it was seen that the area, perimeter, and radius of main tumor structures increased in the following days. Also, it was determined that the main tumor masses showed irregular growth in terms of shape, but the area, perimeter, and radius growth rates for three different days gave different results. The biggest reason for this is thought to be due to the irregular growth of main tumor structures. In addition, the growth values from the second day to the fourth day are quite different from the growth values from the fourth day to the sixth day. This indicates an increase in the growth rate of cancerous cells after the fourth day.

5. CONCLUSIONS

Breast cancer ranks first among cancer types seen in women. This situation has increased the importance of the analysis and interpretation of breast cancer images and so the importance of computer-aided systems in detecting breast cancer is increasing day by day. In the thesis study, images obtained from the mini-Opto tomography platform in the literature were used. The miniOpto tomography platform is a system for creating a new three-dimensional image by reconstructing images taken from different angles. Three-dimensional view of breast cancer and many other microscopic cells can be created with this device. In order to analyze the threedimensional breast cancer cells created for the second, fourth, and sixth days, the 3D images of these cells are primarily divided into layers. There are 50 layers for each day and in our study, ten layers were used for each day. These images were processed in three main processes to be detected and analyzed using Python and OpenCV environments. These are pre-processing, segmentation, and feature extraction steps. In the pre-processing step, noise and unnecessary objects on the images are eliminated using some color transformations and various filters, that is, the image is enhanced. In the segmentation step, the main tumor masses in the image were separated from the image background. For this, thresholding and morphological operations are used. In addition, the boundaries of the main tumor masses were determined and these limits were marked automatically. In the feature extraction step, some formal features of the images were analyzed, that is, area, perimeter, and radius values of the main tumor masses were calculated and these values were compared with each other. Volume values were calculated for three different days based on cross-sectional areas to compare the volumetric growth of the main tumor masses. As a result of the calculation, the volumetric value of the main tumor masses on the second day was 20055 pixels, the volume value on the fourth day was 44466 pixels and the volume value on the sixth day was 82622 pixel. Considering the area, perimeter, and radius measurements for the layers on the second, fourth, and sixth days, it was observed that the highest growth occurred on the sixth day. Especially in the images belonging to cancerous cells, the state of the shape and boundaries of the cancerous structures enable important interpretations about the cancerous structures. In our thesis, the measurements made for the automatic detection of the main tumor masses and the examination of their growth development will contribute to the analysis and interpretation of these images or other images of cancerous structures by experts.

6. RECOMMENDATIONS

In future studies, the methods we use in detecting breast cancer cells and monitoring their growth developments can be tested on mammogram images or on other cancer images. In addition to the area, perimeter, and radius characteristics we use for the main tumor structures in cancerous images, more image features can be extracted. In future work, artificial intelligence-based classification processes will be performed by deep learning or machine learning algorithms using the numerical data we obtained from the image features. Determinations such as growth prediction and cancer type in an image with classification procedures can make important contributions to literature.

REFERENCES

Acar, U., & Bayram, B. Morfolojik Görüntü Filtreleri ile İkonos Görüntülerinden Otomatik Bina Çikarimi. In: TMMOB Harita ve Kadastro Mühendisleri Odası.

Alhadidi, B., Zu'bi, M. H., & Suleiman, H. N. J. I. T. J. (2007). Mammogram breast cancer image detection using image processing functions. *6*(2), 217-221.

Altuntaş, C., & Çorumluoğlu, Ö. (2011). Filtreleme yöntemi ile digital görüntü zenginleştirme ve örnek bir yazılım.

Boateng, K. O., Asubam, B. W., & Laar, D. S. (2012). Improving the effectiveness of the median filter.

Borole, V. Y., Nimbhore, S. S., Kawthekar, D. S. S. J. I. J. o. E. T., & Science, T. i. C. (2015). Image processing techniques for brain tumor detection: A review. *4*(2), 1-14.

Boztoprak, H., Çağlar, M. F., & Merdan, M. J. S. D. Ü., Isparta. (2007). Alternatif morfolojik bir yöntemle plaka yerini saptama.

Cahoon, T. C., Sutton, M. A., & Bezdek, J. C. (2000). *Breast cancer detection using image processing techniques.* Paper presented at the Ninth IEEE International Conference on Fuzzy Systems. FUZZ-IEEE 2000 (Cat. No. 00CH37063).

Çığır, C. (2011). *Histopathological image classification using salient point patterns.* bilkent university,

Deng, G., & Cahill, L. (1993). *An adaptive Gaussian filter for noise reduction and edge detection.* Paper presented at the 1993 IEEE conference record nuclear science symposium and medical imaging conference.

Emmert-Streib, F., & Dehmer, M. J. F. i. g. (2015). Biological networks: the microscope of the twenty-first century? , *6*, 307.

Ferreira, T., & Rasband, W. J. I. F. (2012). ImageJ user guide. *1*, 155-161.

Gong, X., Lin, C., Cheng, J., Su, J., Zhao, H., Liu, T., . . . Zhao, P. J. P. o. (2015). Generation of multicellular tumor spheroids with microwell-based agarose scaffolds for drug testing. *10*(6), e0130348.

Gonzales, R. C., & Woods, R. E. (2002). Digital image processing. In: Prentice hall New Jersey.

Helvie, M. A. (2010). Digital mammography imaging: breast tomosynthesis and advanced applications. *Radiologic Clinics of North America, 48*(5), 917.

Hendrick, R. E., Baker, J. A., & Helvie, M. A. (2019). Breast cancer deaths averted over 3 decades. *Cancer, 125*(9), 1482-1488.

Hooley, R. J., Andrejeva, L., & Scoutt, L. M. (2011). Breast cancer screening and problem solving using mammography, ultrasound, and magnetic resonance imaging. *Ultrasound quarterly, 27*(1), 23-47.

Izadifar, Z., Izadifar, Z., Chapman, D., & Babyn, P. J. J. o. C. M. (2020). An Introduction to High Intensity Focused Ultrasound: Systematic Review on Principles, Devices, and Clinical Applications. *9*(2), 460.

Jeong, Y., Park, D., & Park, K. H. J. s. (2017). PTZ camera-based displacement sensor system with perspective distortion correction unit for early detection of building destruction. *17*(3), 430.

Johnson, S. (2006). *Stephen Johnson on digital photography* (Vol. 13): O'Reilly.

Joseph, R. P., Singh, C. S., Manikandan, M. J. I. J. o. R. i. E., & Technology. (2014). Brain tumor MRI image segmentation and detection in image processing. *3*(1), 1-5.

Julio, R. O., Soares, L. B., Costa, E., & Bampi, S. (2015). *Energy-efficient Gaussian filter for image processing using approximate adder circuits.* Paper presented at the 2015 IEEE International Conference on Electronics, Circuits, and Systems (ICECS).

Karhan, M., Oktay, M., Karhan, Z., & Demir, H. (2011). *Morfolojik görüntü işleme yöntemleri ile kayısılarda yaprak delen (çil) hastalığı sonucu oluşan lekelerin tespiti.* Paper presented at the 6 th International Advanced Technologies Symposium (IATS'11), Elazığ, Türkiye.

Kaushik, D., Singh, U., Singhal, P., & Singh, V. J. I. J. o. C. A. (2013). Medical image segmentation using genetic algorithm. *81*(18), 10-15.

Kaymak, S., Helwan, A., & Uzun, D. J. P. c. s. (2017). Breast cancer image classification using artificial neural networks. *120*, 126-131.

Kumar, T., & Verma, K. J. I. J. o. C. A. (2010). A Theory Based on Conversion of RGB image to Gray image. *7*(2), 7-10.

Li, B., Jevtic, A., Söderström, U., Ur Réhman, S., & Li, H. (2013). *Fast edge detection by center of mass.* Paper presented at the The 1st IEEE/IIAE International Conference on Intelligent Systems and Image Processing 2013 (ICISIP2013).

Lyra, M., Ploussi, A., Georgantzoglou, A., & Ionescu, P. (2011). Matlab as a tool in nuclear medicine image processing. In *MATLAB-A Ubiquitous Tool for the Practical Engineer* (pp. 477-500): InTech.

Makandar, A., & Halalli, B. (2015). Breast cancer image enhancement using median filter and CLAHE. *International Journal of Scientific & Engineering Research, 6*(4), 462-465.

McAndrew, A. J. S. o. C. S., & Mathematics, V. U. o. T. (2004). An introduction to digital image processing with matlab notes for scm2511 image processing. *264*(1), 1-264.

Mohamad, M., Saman, M. Y. M., Hitam, M. S., & Telipot, M. J. T. U. M. T. (2015). A Review on OpenCV.

Mordvintsev, A., & Abid, K. J. R. M. (2017). OpenCV-Python Tutorials Documentation, Release 1. *2*, 2018.

Osborne, C. K., Hobbs, K., Trent, J. M. J. B. c. r., & treatment. (1987). Biological differences among MCF-7 human breast cancer cell lines from different laboratories. *9*(2), 111-121.

Özşen, Ö. (2002). *Matematiksel morfoloji kullanılarak göğüs kanserinin erken teşkisi.* Anadolu Üniversitesi,

Paris, S., Kornprobst, P., Tumblin, J., & Durand, F. (2009). *Bilateral filtering: Theory and applications*: Now Publishers Inc.

Polat, A. (2018). *Compressed sensing based 3D image reconstruction in digital breast tomosynthesis and micro-bioimaging.* Bilişim Enstitüsü,

Polat, A., Hassan, S., Yildirim, I., Oliver, L. E., Mostafaei, M., Kumar, S., . . . Ying, G. J. L. o. a. C. (2019). A miniaturized optical tomography platform for volumetric imaging of engineered living systems. *19*(4), 550-561.

Polat, A., Yildirim, I. J. J. o. X.-R. S., & Technology. (2018). An iterative reconstruction algorithm for digital breast tomosynthesis imaging using real data at three radiation doses. *26*(3), 347-360.

Porikli, F. (2008). *Constant time O (1) bilateral filtering.* Paper presented at the 2008 IEEE Conference on Computer Vision and Pattern Recognition.

Primkhajeepong, C., Phukpattaranont, P., Limsiroratana, S., Boonyaphiphat, P., Kayasut, K. J. S. J. o. S., & Technology. (2010). Evaluation of color based breast cancer cell images analysis. *32*(3).

Raid, A., Khedr, W., El-Dosuky, M., Aoud, M. J. I. J. o. C. S., Engineering, & Technology, I. (2014). Image restoration based on morphological operations. *4*(3), 9-21.

Rao, J., Lin, J., Xu, S., & Lin, S. (2012). *A new intelligent contour tracking algorithm in binary image.* Paper presented at the 2012 Fourth International Conference on Digital Home.

Rogowska, J. J. H. o. m. i., processing, & analysis. (2000). Overview and fundamentals of medical image segmentation. 69-85.

Russ, J. C. (1990). *Computer-assisted microscopy* Springer US.

Sanner, M. F. J. J. M. G. M. (1999). Python: a programming language for software integration and development. *17*(1), 57-61.

Schulze-Hagen, M., Eshghi, N., Müller, J., & Müller-Leisse, C. (2014). *Efficacy of tomosynthesis (DBT) in respect to two different modes (HR vs ST) in a clinical setting. Preliminary results.* Paper presented at the European Congress of Radiology. Vienna, Austria: European Society of Radiology.

Screening, P., & Board, P. E. (2020). Breast Cancer Screening (PDQ®). In *PDQ Cancer Information Summaries [Internet]*: National Cancer Institute (US).

Seyyedi, S., Cengiz, K., Kamasak, M., & Yildirim, I. (2013). An object-oriented simulator for 3D digital breast tomosynthesis imaging system. *Computational and mathematical methods in medicine, 2013*.

Sharma, D., & Jindal, G. (2011). *Identifying lung cancer using image processing techniques.* Paper presented at the International Conference on Computational Techniques and Artificial Intelligence (ICCTAI).

Siegel, R. L., Miller, K. D., & Jemal, A. (2019). Cancer statistics, 2019. *CA: a cancer journal for clinicians, 69*(1), 7-34.

Siegel, R. L., Miller, K. D., & Jemal, A. J. C. a. c. j. f. c. (2020). Cancer statistics, 2020. *70*(1), 7-30.

Sree, S. V., Ng, E. Y.-K., Acharya, R. U., & Faust, O. J. W. j. o. c. o. (2011). Breast imaging: a survey. *2*(4), 171.

Stoitsis, J., Valavanis, I., Mougiakakou, S. G., Golemati, S., Nikita, A., Nikita, K. S. J. N. I., . . . Equipment, A. (2006). Computer aided diagnosis based on medical image processing and artificial intelligence methods. *569*(2), 591-595.

Tomasi, C., & Manduchi, R. (1998). Bilateral filtering for gray and color images In: Sixth International Conference on Computer Vision (IEEE Cat. No. 98CH36271). In: Narosa Publishing House.

Waghulade, K. T., & Yadav, A. K. (2016). *Early breast cancer detection by using image pocessing* Paper presented at the International Conference on Innovative Trends in Engineering Research.

Xie, G., Lu, W. J. I. J. o. E., & Engineering, E. (2013). Image Edge Detection Based On Opencv. *1*(2), 104-106.

Yildiz, K., Demir, Ö., & Ülkü, E. E. J. P. Ü. M. B. D. (2017). Fault detection of fabrics using image processing methods. *23*(7), 841-844.

CURRICULUM VITAE

Cihat Ediz Akbaba was born in Istanbul, TURKEY, in 1988. He graduated from the Electronics-Communication Teaching Department of Marmara University in 2012 and Electrical-Electronics Engineering Department of Osmaniye Korkut Ata University in 2017. He started his master's degree in Electrical-Electronics Engineering at Adana Alparslan Türkeş Science and Technology University in 2018. His current research interests include electronic circuit design, embedded systems, electronic hardware and design, image processing. He has been working as an Electronics Teacher at the Ministry of Education since 2012.

Publications:

Akbaba, C. E. and Polat A., (2020). Detection of breast cancer cells and observation of their development using image processing techniques. *Cukurova 4th International Scientific Researches Conference*, ISBN: 978-625-7954-93-8, Feb 21-23, 2020, Adana, Turkey.

Akbaba, C. E. and Polat A., (2020). Enhancement of the image of a tumor produced by MCF7 breast cancer cells using various image filtering methods. 4^{th} *Asia Pacific International Modern Sciences Congress*, ISBN: 978-625-7687-42-3, Dec. 12-13, 2020, Subic Bay, Philippines.

Akbaba, C. E. and Polat A., (2020). Measuring the object detection success of global and adaptive thresholding methods applied to the breast cancer image. 4^{th} *International 19 May Innovative Scientific Approaches Congress*, ISBN: 978-605-70216-0-1, Dec. 21-22, 2020, Samsun, Turkey.